1 **A first appraisal of the seismogenic and tsunamigenic potential of the**

2 **largest fault systems in the westernmost Mediterranean**

3 Laura Gómez de la Peña[1*], Eulàlia Gràcia[2], Francesco Emanuele Maesano[3], Roberto Basili[3],

4 Heidrun Kopp[1, 4], Cristina Sánchez-Serra[2], Antonio Scala[5], Fabrizio Romano[3], Manuela

5 Volpe[3], Alessio Piatanesi[3], César R. Ranero[2,6]

6

7

8 [1]GEOMAR Helmholtz Centre for Ocean Research, Kiel, Germany.

9 [2]Barcelona Center for Subsurface Imaging, Marine Sciences Institute (ICM-CSIC),

10 Barcelona, Spain.

11 [3]Istituto Nazionale di Geofisica e Vulcanologia (INGV), Rome, Italy.

12 [4]Department of Geosciences, Christian- Albrechts- Universität zu Kiel, Kiel, Germany.

13 [5]Dipartimento di Fisica "Ettore Pancini", Università di Napoli Federico II, Italy.

14 [6]ICREA, Barcelona, Spain.

15

16 * Corresponding author: Laura Gómez de la Peña (lgomez@geomar.de).

17

18 **Highlights:**

19 ● We identify the largest active fault systems of the Alboran Basin.

20 ● Characterization of faults is key for accurate tsunamigenic potential estimations.

21 ● Alboran largest fault systems may generate $M_w > 7$ earthquakes.

22 ● These earthquakes have the potential to generate significant tsunami waves

23 approaching the coast.

24 **Abstract**

25 The westernmost Mediterranean hosts part of the plate boundary between the European and

26 African tectonic plates. Based on the scattered instrumental seismicity, this boundary has been

27 traditionally interpreted as a wide zone of diffuse deformation. However, recent seismic images

28 and seafloor mapping studies support that most of the plate convergence may be accommodated

29 in a few tectonic structures, rather than in a broad region. Historical earthquakes with

30 magnitudes $M_w>6$ and historical tsunamis support that the low-to-moderate instrumental

31 seismicity might also have led to underestimation of the seismogenic and tsunamigenic

32 potential of the area. We evaluate the largest active faults of the westernmost Mediterranean:

33 the reverse Alboran Ridge, and the strike-slip Carboneras, Yusuf and Al-Idrissi fault systems.

34 For the first time, we use a dense grid of modern seismic data to characterize the entire

35 dimensions of the main fault systems, accurately describe the geometry of these structures and

36 estimate their seismic source parameters. Tsunami scenarios have been tested based on 3D-

37 surfaces and seismic source parameters, using both uniform and heterogeneous slip

38 distributions. The comparison of our results with previous studies, based on limited information

39 on the fault geometry and kinematics, indicates that accurate fault geometries and

40 heterogeneous slip distributions are needed to properly assess the seismic and tsunamigenic

41 potential in this area. Based on fault scaling relations, the four fault systems have a large

42 seismogenic potential, being able to generate earthquakes with $M_w>7$. The reverse Alboran

43 Ridge Fault System has the largest tsunamigenic potential, being able to generate a tsunami

44 wave amplitude greater than 3 m in front of the coasts of Southern Spain and Northern Africa.

45 **Keywords:** western Mediterranean, seismogenic potential, tsunamigenic potential, numerical

46 modelling, active faults, active seismic data.

47

48   **1. Introduction**

49   The contact between the European and African tectonic plates along the westernmost

50   Mediterranean is traditionally described as a zone of diffuse deformation with no major plate-

51   boundary fault (Buforn et al., 2004; De Larouzière et al., 1988; Palano et al., 2015). This model

52   is based on the instrumentally-recorded seismicity, which scatters across a broad region (Fig.

53   1). The diffuse plate boundary model infers a ~400-km-wide region of deformation, where

54   numerous faults accommodate convergence between Africa and Europe, and each fault

55   contributes with a comparatively minor amount of slip (e.g., Buforn et al., 2004; Palano et al.,

56   2015). This myriad of modest tectonic structures implies a relatively moderate seismic and

57   tsunami hazard (e.g., Giardini et al., 2014; Basili et al., 2021). Although instrumental seismicity

58   is of moderate magnitude (e.g. IGN seismic catalogue, Stich et al., 2003), there are historical

59   earthquakes inferred to have magnitudes M_w >6 (Fig. 1, Table 1) (IGN, 2013; Mezcua et al.,

60   2004; Palano et al., 2015). These events have long recurrence periods (>1000 years) and

61   involve seismic and tsunami hazards for the region that cannot be characterized only through

62   the instrumental records (<100 years) (Gràcia et al., 2012, 2006). A major issue is that these

63   large historical earthquakes have poorly-defined sources that still are under debate (Fig. 1,

64   Table 1) (Kaabouben et al., 2009; Maramai et al., 2014), but associated tsunamis whose effects

65   have been described along the South Iberian and North African coastal areas. An improved

66   characterization of the local faults is necessary to provide better inputs for local hazard

67   estimates for the densely populated coastal areas of the region.

68   The Alboran region is the westernmost portion of the Mediterranean realm that was formed

69   during the Miocene by processes related to the evolution of a subduction system (e.g., Chertova

70   et al., 2014; Wortel and Spakman, 2000). While the extensional Miocene history of the Alboran

71   Basin is controlled by the slab roll-back and the migration of the subduction front, the Plio-

72   Holocene history (<5.3 Ma) has been governed by the tectonic reactivation of the inherited

73 lithospheric structure in a new plate convergence setting, which remains active today (Gómez

74 de la Peña et al., 2021, 2018). Thus, towards the end of the Messinian (7.2 – 5.3 Ma), the stress

75 framework in the basin changed from an extensional regime to a compressional setting (Gómez

76 de la Peña et al., 2021). However, the Plio-Holocene contractional reorganization of the basin

77 is not pervasively affecting the whole area (e.g., Gómez de la Peña et al., 2021, 2018; Gràcia

78 et al., 2019). Instead, significant deformation is concentrated on a few major tectonic structures:

79 the reverse Alboran Ridge (ARFS) and the strike-slip Carboneras (CFS), Yusuf (YFS) and Al-

80 Idrissi (AIFS) fault systems (Fig. 1, Gómez de la Peña, 2017; Gràcia et al., 2019; Moreno et

81 al., 2017). The location of these >100 km long active faults seems to be conditioned by the

82 lithospheric structure inherited from the basin formation processes, as they have developed at

83 the boundaries between the different crustal domains (Gómez de la Peña et al., 2018, 2020;

84 Gràcia et al., 2019). In addition, studies of the distribution of the offshore seismicity support

85 that the seismic activity is constrained to shallow depths (<20-25 km, Grevemeyer et al., 2015).

86 Thus, a detailed structural characterization of the crustal domains of the Alboran Basin and the

87 reactivated boundaries between them is important to improve the evaluation of the seismogenic

88 and tsunamigenic potential of the fault systems in this tectonically complex area.

89 Previous studies have been performed with limited information of the crustal structure of the

90 fault systems, and the tsunamigenic potential has been modelled with poorly constrained source

91 characteristics (Álvarez-Gómez et al., 2011a, 2011b; Gonzalez et al., 2010). Since then, new

92 seismic images and seafloor high-resolution bathymetry acquired in the westernmost

93 Mediterranean (Fig. 1) have been fundamental to constrain the crustal architecture. In

94 particular, images of the sedimentary and tectonic structure of this area have been key to fully

95 characterize the largest active fault system in the Alboran Basin. Here, using those new

96 observations (Fig. 1), we revise the geometry of the fault systems of the Alboran Basin to

97 constrain fault dimensions, characterize fault parameters (i.e., strike, dip and rake), and perform

98 a preliminary estimation of their associated seismogenic and tsunamigenic potential.

99

100 **2. Geological context**

101 *2.1. Crustal structure*

102 The Miocene extensional processes together with the subduction-related volcanic activity led

103 to the current distribution of three different crustal domains flooring the Alboran Basin (inset

104 of Fig. 1): 1) thin continental crust under the West and North Alboran Basin, similar to the

105 Alboran Domain outcrops onshore, 2) the North African continental crust under the South

106 Alboran Basin, and 3) magmatic-arc crust under the East Alboran Basin (Booth-Rea et al.,

107 2018, 2007; Duggen et al., 2005; Gómez de la Peña et al., 2021, 2018). Towards the east, the

108 Algero-Balearic Basin is floored by oceanic crust (Booth-Rea et al., 2018; Gómez de la Peña

109 et al., 2018).

110 The transition among the different types of crusts are weak inherited zones, in which the Plio-

111 Holocene compressive deformation is focused (Gómez de la Peña et al., 2021, 2018). The

112 largest tectonic structures of the Alboran Basin, namely the ARFS, CFS, YFS and AIFS, >100

113 km long and cutting the entire crust (Fig. 1), are nucleated at the boundaries between the

114 different aforementioned domains (Gómez de la Peña et al., 2018; Gràcia et al., 2019).

115 *2.2. Seismicity of the area*

116 There are two main groups of instrumental seismicity recorded in the Alboran Basin: 1) deep

117 earthquakes under the West Alboran Basin related to the subducted slab (~40-140 km depth)

118 and 2) crustal earthquakes spread over the entire basin (<40 km depth, Mancilla et al., 2015;

119 Martín et al., 2015; Palano et al., 2015, 2013; Stich et al., 2003). In this study, we focus on the

120   crustal seismicity, as the shallow events may have, in principle, a larger seismic and tsunami

121   hazard associated with them. Studies of both the offshore seismicity (Grevemeyer et al., 2015)

122   and the crustal structure (Gómez de la Peña et al., 2020) have shown that most of the offshore

123   earthquakes nucleate at the upper-middle crust (shallower than 20 km depth). The 2016 M_w 6.4

124   earthquake on the AIFS emphasized the seismogenic potential of this area (Gràcia et al., 2019).

125   Due to the slow plate convergence rate (4.5±1 mm/yr, e.g., Nocquet, 2012), these faults

126   possibly have long recurrence intervals for the larger earthquakes that are not fully captured by

127   the instrumental records (Gràcia et al., 2006).

128   The occurrence of earthquakes with M_w >6 is supported by the instrumental and historical

129   events described in this area (Table 1), although the exact location of the historical earthquakes,

130   as well as an accurate estimation of their magnitude, is still not clear (e.g., Kaabouben et al.,

131   2009; Mezcua et al., 2004; Stucchi et al., 2013). In addition to these earthquakes, four tsunamis

132   affecting the South Iberian and North African coasts have been documented (yellow stars in

133   Fig. 1, Kaabouben et al., 2009; Maramai et al., 2014). These tsunamigenic events have been

134   associated with M_w >6 earthquakes (Table 1, e.g., Maramai et al., 2014), but the causative

135   faults are not yet determined. A recent example of a tsunamigenic earthquake in the western

136   Mediterranean is the 2003 Boumerdès earthquake (Mw = 6.8, North Algeria), which generated

137   a tsunami affecting mainly the northern Algeria coast around the Boumerdès Province and the

138   Balearic Islands (Sahal et al. 2009; Selva et al., 2021).

139   As the faults are crustal-scale structures disrupting the basement down to ~20-25 km depth

140   (Gómez de la Peña et al., 2020; 2018), and on the basis of their role as boundaries between

141   different crustal domains and of the seismicity distribution, we assume that the active faults of

142   the Alboran Basin could nucleate earthquakes up to the maximum seismogenic depth. Based

143   on the seismicity distribution, this is around 20 km depth (Grevemeyer et al., 2015).

144 **3. Data and methods**

145   *3.1. Fault analysis and seismic sources parameterization*

146 We used a grid of multichannel seismic reflection (MCS) data (Fig. 1, Table 2), together with

147 selected pre-stack depth-migrated sections and a wide-angle seismic refraction profile showing

148 the velocity structure across the basin (Fig. 1). This MCS grid is formed mainly by datasets

149 collected by the Barcelona-Centre for Subsurface Imaging research group (TOPOMED,

150 EVENT-DEEP, EVENT-SHELF and IMPULS, Fig. 1, Table 2), or processed/reprocessed by

151 the same group (ESCI, CONRAD, CAB, Fig.1, Table 2). For details on the processing flow,

152 see Gómez de la Peña et al. (2018) Supplementary Material. The acquisition, processing and

153 modelling parameters of the WAS profiles are described in Booth-Rea et al. (2018) and Gómez

154 de la Peña et al. (2020).

155 The interpretation of the bathymetry and the MCS profiles of the fault systems allow us to

156 measure their length, width, depth, and strike and dip angles (Figs. 1, 2, 3). The fault traces are

157 correlated among seismic lines using marker horizons (see section 4.1). A detailed description

158 of the seismic stratigraphy of the Alboran Basin is presented in Gómez de la Peña et al. (2021).

159 In particular, in this study we used four marker horizons: the sea-floor horizon when it is

160 disrupted, the Messinian surface (indicated as "M" in Figures 2 and 3, 5.33 Ma), the basement

161 top (volcanic -VB- or metamorphic -Mt.B- depending on the area and also variable in age), and

162 the crustal reflectivity when it is observed. A detailed description of the horizons' displacement

163 and deformation is given in section 4.1 "Fault Geometries". The displacement of the horizons

164 is consistent across all the seismic profiles, and together with the continuous bathymetric

165 expression and the crustal dimensions of the analysed fault systems, supports the continuity of

166 the fault planes. Based on our interpretation, we correlated the fault segments among different

167 sections and performed a Delaunay triangular interpolation to create 3D models of the fault

168   planes, providing the first realistic geometry of the selected faults in the area (Fig. 4). As the

169   seismic grid is formed by time-migrated profiles, the fault surfaces have been first interpreted

170   in the time domain. Once the fault surface mesh was interpolated, we performed the 3D time-

171   depth conversion of the mesh (Maesano and D'Ambrogi, 2017) using a four-layer model. The

172   layers are defined using three horizons (Figs. 2, 3): the seafloor, the Messinian top (M) and the

173   basement top (top of the volcanic or metamorphic basement, depending on the area). Based on

174   1) the existing tomographic velocity models inverted from wide-angle seismic data along and

175   across the Alboran Basin (profiles WESTMED at Fig. 1, Booth-Rea et al., 2018; Gómez de la

176   Peña et al., 2020) and 2) the velocity models used for the Pre-Stack Depth Migration of two

177   MCS profiles (Gómez de la Peña, 2017), we assigned a P-wave velocity of 1500 m/s to the

178   water layer, 2100 m/s for the Plio-Holocene sediments, 2700 m/s for the Miocene sediment

179   and 5000 m/s for the basement. Finally, the accuracy of time-depth conversion has been

180   checked comparing the obtained fault meshes with the interpreted fault traces at the pre-stack

181   depth-migrated sections (Gómez de la Peña, 2017).

182   We derived the fault rake components on each triangular element of the mesh by assuming an

183   average regional NW-SE convergence azimuth (Fig. 1, Nocquet, 2012) without slip

184   partitioning. In order to estimate the earthquake magnitude M_w and average slip associated with

185   the largest rupture area (defined by length and width of the fault measured for each fault

186   system), we have applied the empirical scaling laws proposed by Leonard (2014) for crustal

187   earthquakes (Table 3).

188   To enhance the representation of the coseismic rupture and assess how the slip distribution may

189   affect tsunamigenesis, we also tested one scenario featuring a heterogeneous slip distribution.

190   The heterogeneous slip distributions have been calculated through a composite stochastic

191   source models (Ruiz et al., 2011; Zeng et al. 1994) based on the random distribution of

192   overlapping circular sub-asperities whose size and number are defined to ensure that the slip

193   amplitude decays as k^2 at large wavenumber with k representing the wavenumber domain. The

194   distance among the grid-nodes and hence the proper definition of the circular sub-asperities is

195   efficiently modelled through the multi-lateration scheme presented in Herrero and Murphy

196   (2018). This technique has been already tested and applied for tsunami scenario computation

197   and for probabilistic tsunami hazard purposes (Scala et al., 2020, Basili et al., 2021).

198   *3.2. Numerical tsunami simulations*

199   After retrieving the geometries (Fig. 4) and the parameters for each fault system (Table 3), we

200   calculated the associated tsunami scenario. When the rupture area associated with the estimated

201   earthquake M_w is not sufficient to cover the entire fault, the rupture area has been placed as

202   shallow as possible to maximize the seafloor displacement, which represents the initial

203   condition for the tsunami propagation. Numerical tsunami simulations were performed using

204   the Tsunami-HySEA nonlinear shallow water GPU-optimised code, developed by the

205   EDANYA Group of the University of Malaga, Spain (de la Asunción et al., 2013). The

206   computational time-step is automatically set by the code during the simulation (0.2 s on average

207   for the scenarios simulated in the present study, using a value of 0.7 for the Courant–

208   Friedrichs–Lewy condition); we adopt a friction Manning coefficient of 0.03, where the

209   duration of each tsunami propagation is 2 hours. To propagate the tsunami, we used the

210   EMODnet bathymetry model that has a spatial resolution of 1/16 arc minutes (i.e., ~115 meters,

211   EMODnet Bathymetry project, www.emodnet-bathymetry.eu). We have calculated the

212   maximum wave amplitude distribution and the tsunami travel time for each tsunami scenario

213   (Figs. 6-10).

214

215   **4. Results**

216   *4.1. Fault geometries*

217   The most prominent structure of the Alboran Basin is the Alboran Ridge (Figs. 1, 2). This

218   morphologic high shows >2 km of uplift, reaching the surface and forming the Alboran Island

219   (Fig 1). This high has been uplifted by the ARFS (Fig. 2). The ARFS is a south-dipping thrust

220   fault rooted at the Mohorovicic' discontinuity (Moho), and formed by a ramp and a flat segment

221   at its deepest part (Fig. 2). North of the ARFS, the crust is ~7 s Two Way Travel Time (TWTT)

222   (Fig. 2); while south of it is ~9 s TWTT (Fig. 2), supporting the crustal character of this

223   structure. Towards the west, the ARFS is disrupted by the AIFS (Figs. 1, 2c) and towards the

224   east, evolves into a transpressive structure (Fig. 2a) that seems to connect with the YFS (Fig.

225   1). In its eastern portion, the ARFS is reaching the seafloor, cutting the most recent Plio-

226   Holocene sediments and producing a vertical step in the Messinian (M) horizon of >1.5 s

227   TWTT (CMPs ~4000, Fig. 2a). At the central section, the ARFS is a blind thrust (Fig. 2b CMP

228   ~8000). However, the Plio-Holocene units are involved in the folding related to the

229   deformation, suggesting that it is active (Fig. 2b, CMPs 8000-4000). The vertical step measured

230   on the M horizon is ~1.5 s TWTT (Fig. 2b). We interpreted secondary faults disrupting the

231   south side of the Alboran Ridge, with a comparatively minor deformation associated (Fig. 2b,

232   CMP ~5500). At the western end, the ARFS is cut by the AIFS (Figs. 1, 2c). In this area, the

233   ARFS also shows signs of activity, cutting the entire sedimentary sequence and deforming the

234   Plio-Holocene sediments (Fig. 2c, CMPs 3500-1500).

235   The CFS is an onshore-offshore strike-slip fault system, 140 km long (~90 km offshore) (Fig.

236   1). It is a sub-vertical fault (Fig. 3a, CMP ~18000) that separates domains with different crustal

237   thickness: toward the west, the Moho is interpreted at ~11 s TWTT, defining a ~9 s TWTT

238   thick crust, while towards the east, the Moho is interpreted at 8 s TWTT, delineating a ~7 s

239   TWTT crust. The CFS is an active fault, reaching the sea-floor surface and deforming the most

240   recent sediments (Fig. 3a, CMPs 17500-18500). The CFS has an approximately constant strike

241   (230 °, Table 3).

242   The YFS is a sub-vertical strike-slip fault system ~145 km-long (Fig. 1) with an approximately

243   constant strike (107º, Table 3). Although it is formed by two segments in its shallower section

244   (Figs. 1, 3b), these two segments connect at depth into a single fault plane (Fig. 3b, CMPs

245   7000-9000). Between the two segments, the Yusuf pull-apart Basin is formed, filled up mainly

246   with Plio-Holocene sediments (Fig. 3b, CMPs 7000-9000). The YFS affects the entire crust, as

247   demonstrated by the different crustal thicknesses observed at the two sides of the fault: ~12 s

248   TWTT south of the YFS and ~6 s TWTT north of it (Fig. 3b). Both fault segments reach the

249   sea-floor (Fig. 3b, CMPs ~7000 and ~8750), and the Plio-Holocene sediments are deformed

250   by the fault activity, supporting that it is an active structure.

251   The AIFS is a strike-slip fault, 105 km long, and it is also cutting the entire crust (Fig. 2b).

252   Along its trace, the AIFS forms negative and positive flower structures (Fig. 2b, CMPs ~4000-

253   3500) that are deforming the Plio-Holocene sedimentary sequence. Thus, we interpreted this

254   fault as an active structure. It is a sub-vertical fault (Fig. 2b) with an approximately constant

255   strike (Fig. 1, 20º, Table 3).

256   Our grid of seismic data allowed us to characterize the fault geometries, especially at deeper

257   crustal levels. Based on the fault trace interpreted at the MCS profiles (Figs. 1, 2), the ARFS

258   has been modelled building a 3D-triangular mesh accounting for its complex geometry (Figs.

259   4, 5). To estimate the ARFS parameters, the geometry of the fault has been taken into account,

260   as the ARFS has variable strike, dip and rake (Fig. 5). The fault parameters, retrieved after the

261   time-depth conversion, are shown in Table 3 (see Supplementary Data for details). To further

262   support the importance of the fault characterization, we show a tsunami scenario comparing

263   the results of the tsunami model using a planar fault approximation of the ARFS geometry and

264   a realistic fault geometry in the Supplementary Material (Fig. S1). For the strike-slip faults we

265   adopted a planar geometry, as this approximation accounts for a realistic fault geometry when

266   the fault has an almost constant dip and strike (Figs. 2c, 3, 4). For these fault systems, all the

267   parameters are kept fixed apart from the rake angle (Table 3; see section 4.2.2).

268   In accordance with the fault dimensions and the estimated seismic parameters, these faults can

269   produce earthquakes with M_w 7.7 for the ARFS, and between 7–7.3 for the strike-slip systems

270   (Table 3).

271   **4.2. Tsunami simulations**

272   *4.2.1. Thrust fault: Alboran Ridge Fault System*

273   We first considered a M_w 7.7 earthquake with uniform slip (2.66 m, Table 3) and two possible

274   scenarios to test the influence of the rake on the resulting maximum tsunami wave amplitude.

275   Thus, we considered a scenario with constant rake (80º, Figs. 6c) and another one with variable

276   rake (~30º-140º, Figs. 5c, 6d). The constant rake scenario considers the average rake value,

277   taking into account the regional convergence and the average strike of the fault plane, while

278   the variable rake scenario accounts for the ARFS strike variations (Fig. 5). The hypothesis of

279   a variable rake is due to the curved structure of the ARFS, as changes in the fault strike can

280   result in a variability of the kinematics from pure to oblique thrusting (Fig. 5c). The results do

281   not highlight a systematic predominance, in terms of maximum wave amplitudes, of a scenario

282   with respect to the other, along the coastal points (Fig. 6). We observe that the tsunami scenario

283   adopting a variable rake has relatively larger wave amplitudes in South Spain between Málaga

284   and Calahonda (points 4 and 3, Fig. 6b) and in the North African coast west to Melilla (point

285   10, Fig. 6b), whereas adopting a constant rake highlights larger values in the southeastern coast

286   of Spain around Almeria and in the North African coast east to Melilla (points 2 and 10, Fig.

287   6b). The maximum difference at the coastal points is observed at Almeria and Melilla (~1 m,

288   points 2 and 10, Figs. 6a, b). Both scenarios show that the most exposed areas are close to

289   Melilla on the North African coast (point 10), where the models support a maximum wave

290   amplitude of >2.5 m, and between Málaga and Almería on the South Spanish coast (points 2-

291   4), with a maximum wave amplitude of 3-6 m (Fig. 6).

292   In a second experiment, we tested the influence of the slip distribution by focusing only on

293   potential ruptures hosted by the ARFS thrust ramp, and we considered a maximum M_w 6.8

294   earthquake. Thus, we run two different simulations, considering a uniform (Fig. 7a), and a

295   heterogeneous slip distribution (Fig. 7b) for similar rupture areas with constant rake. The

296   results show that the stochastic slip distribution used in this test-case produces generally larger

297   maximum wave amplitudes compared with the uniform slip scenario (Fig. 7c). An opposite

298   behaviour is observed in the stretch of Spanish coast between Calahonda and Almería (points

299   3 and 2), where larger values result from the homogeneous case due to the easternmost part of

300   the fault model that features larger slip values (Fig. 7a) than the stochastic scenario (Fig. 7b).

301   Although the absolute difference between the maximum wave amplitude modelled in the two

302   scenarios is relatively small (<0.5 m), the relative size of the wave amplitude modelled with

303   heterogeneous slip with respect to the homogeneous slip generally represents an increase up to

304   ~40% (west of point 3, Fig. 7c). Similar to the M_w 7.7 scenarios, the most affected areas are at

305   the South Spanish coast, even if the smaller earthquake magnitude contributes to a reduction

306   in the maximum wave amplitude (Fig. 7). The estimated tsunami arrival time for both the cases

307   is in the range of ~10-20 minutes along the Southern Spain and Northern Africa coasts (Figs.

308   6, 7).

309   *4.2.2. Strike-slip faults: Carboneras, Yusuf, and Al-Idrissi Fault Systems*

310   For the CFS we considered three scenarios, that is a purely left-lateral strike-slip mechanism

311   (rake=0, Fig. 8b), and a small normal/inverse component (i.e., rake=10°, 350°, Figs. 8c-d). Due

312   to the proximity of the source to the coastline, this is especially relevant for the Southeast

313   Spanish coast. The maximum wave amplitude (>0.3 m) is observed when considering a rake

314   of 350° (Figs. 8a, c).

315   We follow a similar approach for the YFS, considering a purely right-lateral strike-slip

316   mechanism (rake = 180°) and a rake of 190° and 170° assuming the YFS having a vertical

317   component behaviour (i.e., transtension at the Yusuf pull-apart basin, Fig. 3b). Even if

318   relatively small, the oblique component of the slip direction introduced for the latter scenarios

319   contributes to generate larger tsunami wave amplitudes (compare Fig. 9b with Figs. 9c, d). In

320   particular, the scenario adopting a rake of 190° features wave amplitude >0.4 m along the North

321   African coast (point 11, Fig. 9a), whereas the scenario with a rake of 170° features wave

322   amplitude between 0.8 and 1.5 m along the South Spanish coast around the Almeria area (point

323   2, Fig. 9a). The maximum wave amplitude estimated considering a pure strike-slip scenario is

324   <0.2 m (Fig. 9a).

325   Finally, we modelled a tsunami scenario for the AIFS fault that features a dominant left-lateral

326   strike-slip mechanism (rake = 25°, based on the 2016 M_w 6.4 earthquake parameters, Gràcia et

327   al., 2019). In this case the tsunami affects particularly the western side of both Southern Spain

328   and Northern Africa coasts with maximum wave amplitudes of 0.5 m close to Ceuta (North

329   African coast, point 8 Fig. 10a) and La Línea de la Concepción (South Spanish coast, point 7

330   Fig. 10a).

331   Even with specific different patterns due to the tsunami source locations, the estimated first

332   tsunami arrival times in all of the scenarios presented in the present study are in the range of

333   ~10-20 minutes (Figs. 8, 9, 10).

334

335   **5. Discussion**

336   *5.1. Fault characterization: influence in the numerical tsunami simulations*

337   The main outcome of this study is the characterization of the fault geometry using a grid of

338   modern MCS profiles (Fig. 1). This grid allows us to reconstruct the fault model complexities

339   at their shallower and deeper parts, and thus, to incorporate realistic rupture parameters into

340   tsunami scenarios. Previous studies were based on the geodynamic setting of the area

341   (González et al, 2010) or had limited information on the fault geometry and kinematics

342   (Álvarez-Gómez et al., 2011a, 2011b). Thus, in these previous studies, not all the sources were

343   considered (i.e., ARFS, AIFS), and the fault and source parameters were approximated from

344   the bathymetry and scarce geophysical data.

345   The MCS profiles support that the ARFS, CFS, YFS and AIFS are active faults, deforming the

346   Pliocene-Holocene sedimentary sequence and even disrupting the sea-floor (Figs. 1, 2, 3),

347   which agrees with previous studies (Gràcia et al., 2019; Martínez-García et al., 2013; Moreno

348   et al., 2017; Perea et al., 2020). Since our goal was the geometrical reconstruction of the faults

349   and the tsunami simulations, we did not perform a quantification of the fault slip-rates which

350   would be necessary to fully incorporate the modelled faults into seismic and tsunami hazard

351   studies.

352   One of the major differences between this work and the previous interpretation for this area

353   regards the ARFS. This structure was interpreted as a transpressive fault system (e.g., Martínez-

354   García et al., 2013), although modern MCS profiles revealed it as a reverse fault rooted at the

355   Moho (Gómez de la Peña, 2017; Gómez de la Peña et al., 2018). Previous interpretations placed

356   the master transpressive faults at the northern and southern sides of the Alboran Ridge

357   (d'Acremont et al., 2020; Martínez-García et al., 2013). The southern fault is observed in some

358   of the MCS profiles but we interpreted it as a secondary fault with a size that is not comparable

359   to the ARFS, that is the main thrust lifting the Alboran Ridge (Fig. 2). Hence, this is the first

360   study considering the ARFS as a crustal-scale thrust, being one of the main potentially

361   tsunamigenic structures in the Alboran Basin area.

362   In particular, Álvarez-Gómez et al. (2011a, b) described the tectonic structure of the Alboran

363   Ridge by three different fault segments, being two of them left- and right-lateral strike-slip

364   faults (north and south branches, respectively) with a 10° compressive component, and the

365   third one a reverse fault. This reverse fault extended for a length of 37 km, while modern

366   seismic data revealed it as a ~120 km fault (Figs. 1, 2, 4, 5). The maximum fault depth

367   considered in previous studies is between 11-13 km, while modern seismic data support that

368   the ARFS is rooted at ~15 km depth (Gómez de la Peña et al., 2018). The estimated maximum

369   earthquake magnitude to the Alboran Ridge faults range between 6.7-7.1, while with the fault

370   parameters described in this survey a realistic maximum earthquake magnitude can be larger

371   than M_w 7.7. The comparison of our results with the tsunami scenarios previously modelled

372   considering the Alboran Ridge a transpressive structure (Álvarez-Gómez et al., 2011a)

373   highlights that, while the areas affected by the higher amplitude waves are similar in both

374   studies, there are some differences in terms of maximum wave amplitudes. Indeed, considering

375   the south fault of the Alboran Ridge as the master transpressive fault, Álvarez-Gómez et al.

376   (2011a) reported maximum wave amplitudes of 1-1.5 m along the 10 m isobath (using a

377   bathymetry with a spatial resolution of 30 arc-sec), while considering the ARFS as the master

378   reverse fault of the system (as considered in the present study) we obtained larger values with

379   differences >1.5 m (up to 4 m, measured on the 10 m isobath).

380   A specific test was performed to check how the rake angle may affect the tsunami. Despite the

381   ARFS slightly curved geometry, which suggests a change of strike and rake along the fault

382   trace (Figs. 1, 2, 5a), using constant or variable rakes yields similar tsunami wave patterns

383   (Figs. 6a, b). The rake variations, accounting for more oblique thrusting at the Eastern and

384   Western ends of the Alboran Ridge (Figs. 2c, 5c), have the main effect of decreasing the

385   maximum wave amplitude (Figs. 6a, b). An additional test was performed to check how the

386   slip distribution may affect the tsunami with respect to a coseismic homogeneous dislocation

387   in the same fault area (Fig. 7). The results show that in the near field of the tsunami source, the

388   slip distribution produces larger maximum wave amplitudes compared with the uniform slip

389   scenario (Fig. 7c). This result was expected (e.g., Geist, 2002), but for a robust tsunamigenic

390   potential analysis it would be necessary to compute a much larger number of scenarios based

391   on stochastic slip modelling for different magnitudes and slip patch locations (e.g., Murphy et

392   al., 2016; Scala et al., 2020).

393   Regarding the strike-slip systems, a good agreement is found when comparing the maximum

394   tsunami wave amplitudes resulting from the CFS strike-slip fault modelling in both our study

395   and the one by Álvarez-Gómez et al. (2011a). In both studies the CFS is interpreted as a left-

396   lateral strike-slip fault, with a small transpressive component (5°, Álvarez-Gómez et al., 2011a,

397   2011b) or transpressive and transtensive components (±10° variability, this work). Our data

398   allows interpreting the CFS down to 20 km depth (Gómez de la Peña et al., 2018), while in

399   previous studies it was modelled to 11 km depth (Álvarez-Gómez et al., 2011a, 2011b).

400   However, this change produces minor differences in the tsunami modelling results.

401   On the other hand, some differences appear relatively to the YFS system, due to a different

402   fault modelling. Indeed, due to its bathymetric expression, the YFS was modelled as two

403   independent, right-lateral strike-slip fault systems in previous studies (Álvarez-Gómez et al.,

404   2011a). Here, thanks to the high-penetration seismic images that show that the two branches

405   of the YFS join at depth (Fig. 3b), we have considered the entire YFS as one single fault system.

406   This change results in an increment of the total fault length, and increases the maximum wave

407   amplitude by ~0.2 m on the 10 m isobath (point 11, Beni Saf, Fig. 9, Álvarez-Gómez et al.,

408   2011a).

409   Different from the CFS and YFS faults, the AIFS tsunamigenic potential has not been modelled

410   before. Our tsunami simulation shows a relatively lower tsunamigenic potential for this fault

411   system (Fig. 10) with respect to the other fault systems analysed in the present study.

412   Due to the uncertainty in the regional convergence value (e.g., Serpelloni et al., 2007), the

413   variability of the stress framework in the area (e.g., Echeverria et al., 2013; Palano et al., 2015)

414   and the lack of focal mechanism associated with these faults, we assigned an uncertainty to the

415   rake value of the CFS and YFS of ±10º. This small transpressive/transtensional component

416   cannot be discarded with the available data, and considerably increased the amplitude of the

417   maximum wave, being more than double at some points (Figs. 8a, 9a). This is especially

418   noticeable at the closest coastal areas for each fault (Figs. 8, 9). This difference may translate

419   into non-negligible higher differences due to amplification of the tsunami wave when reaching

420   the coast.

421   Collectively, our results are a first attempt to highlight how the fault characterization can be

422   relevant to improve the definition of the tsunamigenic potential of the tectonic structures in the

423   Alboran Basin. Although the new data allowed us to better constrain the fault geometry, other

424   important parameters, such as the rake, have a relatively large uncertainty and may influence

425   the resulting tsunami model, especially when considering an oblique component for the major

426   strike-slip faults.

427   *5.2. Seismogenic and tsunamigenic potential*

428   The seismogenic potential of the faults of the Alboran Basin has been not fully addressed

429   because of 1) the recorded instrumental seismicity which is moderate (Palano et al., 2015; Stich

430   et al., 2003), 2) the possibly long recurrence periods for the larger earthquakes (Gràcia et al.,

431   2006), and 3) the lack of constraints on the deep structure of the basin and thus of the tectonic

432   structure (Gómez de la Peña et al., 2020, 2018). Our results support that the main faults of the

433   Alboran Basin may be able to generate large tectonic events with M_w >7 (Table 3).

434   The largest earthquake instrumentally recorded in this area is the Al-Idrissi earthquake (M_w

435   6.4, 2016, Gràcia et al., 2019). This earthquake was nucleated on the AIFS (Gràcia et al., 2019).

436   For this fault, we modelled a fault geometry which can theoretically host earthquakes as large

437   as M_w 7, according to the adopted scaling relationship (Leonard, 2014), which agrees with the

438   M_w 6.4 2016 earthquake (Table 3). The occurrence of the 2016 earthquake supports that these

439   fault systems, being engendered at the boundary between different crustal domains, are highly-

440   continuous structures and that a seismic event may be able to rupture a large area (Gràcia et

441   al., 2019). Thus, even if these fault systems have long recurrence periods, their seismogenic

442   potential should be further explored.

443   In addition, the scenarios computed in our work are comparable with the largest historical

444   seismicity observed in the area (e.g., Mezcua et al., 2004; Palano et al., 2015) which also

445   produced tsunami effects (e.g., Maramai et al., 2014 and references therein) (Table 1). The

446   specific faults activated during these historical earthquakes and tsunamis, as it is often the case,

447   remain undetermined or only poorly defined (e.g., Kaabouben et al., 2009; Maramai et al.,

448   2014; Mezcua et al., 2004). Although finding the source of a particular event is beyond the

449   scope of this study, we have shown that the main tectonic structures of the Alboran Basin

450   (ARFS, CFS, YFS and AIFS) could potentially host these earthquakes and generate the

451   subsequent tsunamis. In particular, our simulations show that the greatest tsunami in this area

452   could be generated by the ARFS, but also the tsunami scenarios related to the CFS and the YFS

453   could feature maximum wave amplitudes with values of the order of 0.5 m affecting the closest

454   coastal areas.

455   Among the structures analysed in the present study, the ARFS expresses the highest

456   seismogenic and tsunamigenic potential, being able to generate an earthquake up to M_w 7.7 and

457   a tsunami with a maximum wave amplitude >3 m along the 10 m isobath, considering a rupture

458   area extending over the entire fault plane (Table 3, Fig. 6). Considering a rupture area restricted

459   to the ramp of this thrust, the ARFS may generate an earthquake M_w 6.8 and tsunami waves

460   with amplitude >1 m at the 10 m isobath in front of the Southern Spain coast (Table 3, Fig. 7).

461   Similar to the AIFS, the ARFS is located in between two different types of crust (Fig. 2, Gómez

462   de la Peña et al., 2020, 2018). The relief associated with this structure, the Alboran Ridge, is a

463   continuous high >100 km long (Fig. 1). Although these factors may support the existence of a

464   continuous deformation area, further analyses of the fault's seismogenic behaviour and

465   accurate location of the offshore larger seismic events (recorded and historical) are needed to

466   determine whether the ARFS is prone to rupture as a whole.

467   The strike-slip systems could also host significant earthquakes (Table 3), as confirmed by the

468   M_w 6.4 earthquake nucleated on the AIFS in 2016 (Gràcia et al., 2019). However, given their

469   kinematics, the associated tsunamigenic potential is low compared to ARFS, at least for the

470   scenarios considered here. Indeed, the vertical displacement of the seafloor associated with

471   these structures is limited and the contribution of the horizontal deformation in terms of

472   tsunamigenesis is relevant only in particular cases such as shallow dipping fault planes

473   (Tanioka and Satake, 1996) or supershear ruptures (Elbanna et al., 2021). The maximum wave

474   amplitudes calculated for the strike-slip faults are in the order of 0.3 – 0.5 m, reaching up to

475   1.5 m at particular points (Figs. 8a, 9a, 10a). Due to the influence of poorly constrained

476   parameters (i.e., rake) in the modelled tsunami scenario, further characterization of the strike-

477   slip fault systems is recommended.

478   In this study, we independently studied the reverse ARFS and the strike-slip CFS, YFS and

479   AIFS. However, the ARFS and the YFS has a compatible kinematics and, based on their

480 surface and depth structure, these two fault systems may be linked (Figs. 1, 2a, 3b) through a

481 transpressive zone connecting the ARFS thrust with the strike-slip YFS (Fig. 2a, Gómez de la

482 Peña, 2017). This consideration is also supported by the computed rake value where we observe

483 that the eastern termination of the ARFS features a significant oblique component (Fig. 5c).

484 Complex ruptures involving different fault segments with different kinematics have been

485 observed in other areas (e.g., 2016 M_w 7.8 Kaikoura earthquake, Ulrich et al., 2019; 2019 M_w

486 7.1 Ridgecrest earthquake, Chen et al., 2020). However, hypothesizing that a seismic rupture

487 could involve both ARFS and YFS implies a complex rupture model that requires a further

488 analysis of the fault deformation, as well as a complex analysis of the slip distribution and of

489 the kinematics of the thrust-transpression-strike-slip system.

490 Here, we presented an example of how to combine the main elements of a seismogenic and

491 tsunamigenic analysis with the main tectonic structures of the Alboran Basin that for the first

492 time considers a realistic fault geometry. The improvement in the geological knowledge

493 reduces the uncertainty of the seismic source parameters and the epistemic uncertainty in the

494 tsunami forward modelling; however, in order to fulfil the seismic and tsunami hazard

495 assessments of the westernmost Mediterranean coastal areas, a Probabilistic Seismic and

496 Tsunami Hazard Assessment is needed (e.g., Basili et al., 2021, Gerstenberger et al., 2020).

497 The importance of well-constrained fault geometries and slip distribution in tsunami modelling

498 (Tonini et al., 2020; Serra et al., 2021), ground-shaking modelling (Passone and Mai, 2017),

499 and probabilistic seismic and tsunami hazard studies have already been demonstrated (e.g.,

500 Goda et al., 2014; Scala et al., 2020). Thus, future hazard studies, and especially those

501 conducted at a regional or local scale, would be further improved by using the more realistic

502 fault geometries available, and considering a suite of stochastic slip distributions (e.g., Passone

503 and Mai, 2017; Scala et al., 2020) to produce accurate seismic and tsunami hazard models. For

504 the Alboran region, we propose the use of at least the main active structure of the area (ARFS,

505 CFS, YFS and AIFS) presented in this study.

506

507 **6. Conclusions**

508 Modern seismic images and high-resolution seafloor maps have provided the observations to

509 revise the geometry of the largest active fault systems of the Alboran Basin. The new mapping

510 of the structures allows us to create 3D realistic fault models, which have been used for the

511 first time as input for the seismogenic and tsunamigenic potential estimations. Comparison

512 with previous tsunami models of the area, done with limited knowledge of the tectonic

513 structure, highlights the key role of detailed fault characterization.

514 We have estimated earthquake magnitudes that might be hosted by the main active fault

515 systems of the Alboran Basin based on the new characterization. The reverse ARFS may

516 produce earthquakes as large as $M_w 7.7$, and the strike-slip system of CFS M_w 7.1, YFS M_w 7.3

517 and AIFS M_w 7.0.

518 In our scenarios, the highest tsunamigenic potential is associated with reverse slip along the

519 ARFS, with estimated maximum wave amplitudes >3 m on the 10 m isobath. The tsunamigenic

520 potential of the strike-slip faults in the investigated cases is lower than that for the ARFS (<1.5

521 m wave amplitude on the 10 m isobath), but due to their proximity to the coast, the influence

522 of poorly constrained parameters such as the rake, and possible local effects and coastal

523 amplification processes that are not considered in this study, the tsunamigenic potential of the

524 strike-slip structures analysed here might have been underestimated.

525 The complexity of megathrust earthquake ruptures has already been addressed in several

526 studies. Our results show the importance of the fault first-order characterization when

527 estimating the seismic and tsunamigenic potential also in the case of crustal earthquakes.

528   Accounting for realistic fault geometries and seismic parameters is especially relevant when

529   the faults feature a complex geometry (e.g., the ARFS) and future studies should also include

530   other physical aspects of the tsunami generation, such as shallow slip amplification or

531   kinematic seafloor deformation, which are still under explored in the case of crustal faults.

532

550

551   **Data availability**

552 The data (3D complex mesh of the ARFS and rake values, and the resulting grid files of the

553 tsunami simulations containing the maximum wave amplitude) are archived at PANGAEA

554 repository (https://doi.pangaea.de/10.1594/PANGAEA.xxxxxxx) (the full link to download

555 these data will be given once the paper has been accepted).

556

557 **Figure captions:**

558 **Figure 1:** Bathymetric map of the westernmost Mediterranean (Alboran Basin, Ballesteros et

559 al., 2008; Gómez de la Peña et al., 2016; Gràcia et al., 2012, 2006 and GEBCO compilation).

560 Location of the MCS and WAS profiles is shown (colour lines, see map legend with the details),

561 as well as the location of the main tectonic structures (modified after Gràcia et al., 2019). The

562 studied fault systems are depicted in red. Instrumental seismicity limited to crustal depths (<30

563 km, IGN seismic catalogue) and historical earthquakes and tsunamis (Kaabouben et al., 2009;

564 Maramai et al., 2014; Palano et al., 2015) are displayed (see details in the map legend). The

565 numbers show the location of the coastal cities taken as reference. Inset: location of the study

566 area and crustal domains (modified from Gómez de la Peña et al., 2018). ARFS: Alboran Ridge

567 Fault System, CFS: Carboneras Fault System, YFS: Yusuf Fault System, AIFS: Al-Idrissi Fault

568 System.

569 **Figure 2:** The ARFS and AIFS. **a)** Eastern termination of the ARFS (Event-Deep Leg 2 cruise),

570 **b)** Central section of the ARFS (TopoMed cruise, modified from Gómez de la Peña et al.,

571 2018), **c)** Western termination of the ARFS and AIFS (TopoMed cruise, modified from Gràcia

572 et al., 2019). The main fault trace of the studied fault systems is marked in red. PlioH: Plio-

573 Holocene sediments, Mio: Miocene sediments, M: Messinian top, V: volcanics, VB: volcanic

574 basement, Mt.B: metamorphic basement, ICR: Intra-crustal reflectivity.

575   **Figure 3:** The **a)** CFS and **b)** YFS (modified from Gómez de la Peña et al., 2018). The main

576   fault trace of the studied fault systems is marked in red. PlioH: Plio-Holocene sediments, Mio:

577   Miocene sediments, M: Messinian top, V: volcanics, VB: volcanic basement, Mt.B:

578   metamorphic basement, ICR: Intra-crustal reflectivity.

579   **Figure 4:** 3D modelled grids of the ARFS, CFS, YFS and AIFS.

580   **Figure 5:** Details of the ARFS 3D complex mesh: **a)** strike variations, **b)** dip variations and **c)**

581   rake variations.

582   **Figure 6:** Tsunami simulation for the ARFS considering a uniform slip distribution and a slip

583   of 2.66 m (M_w 7.7 earthquake). The colour scale shows the maximum wave amplitudes; white

584   contour lines (10 minutes intervals) represent the estimated tsunami travel times. **a)** Maximum

585   wave amplitudes along the South Spanish and North African coasts, extracted at the 10 m

586   isobath. Selected locations are displayed for reference (see Figure 1). **b)** Results of the tsunami

587   simulation using constant rake and **c)** variable rake. The numbers show the location of the

588   coastal cities taken as reference: 1: Cartagena, 2: Almería, 3: Calahonda, 4: Málaga, 5:

589   Fuengirola, 6: Marbella, 7: La Línea de la Concepción, 8: Ceuta, 9: Alhucemas, 10: Melilla,

590   11: Beni Saf.

591   **Figure 7:** Tsunami simulations for the ARFS considering **a)** a homogeneous and **b)** a

592   heterogeneous slip distribution for a M_w 6.8 earthquake. The colour scale shows the maximum

593   wave amplitudes; white contour lines (10 minutes intervals) represent the estimated tsunami

594   travel times. **c)** Maximum wave amplitudes along the South Spanish and North African coasts,

595   extracted at the 10 m isobath. Selected locations are displayed for reference (Fig. 1). Tsunami

596   simulation results for **d)** uniform slip and **e)** heterogeneous slip. The numbers show the location

597   of the coastal cities taken as reference: 1: Cartagena, 2: Almería, 3: Calahonda, 4: Málaga, 5:

598   Fuengirola, 6: Marbella, 7: La Línea de la Concepción, 8: Ceuta, 9: Alhucemas, 10: Melilla,

599   11: Beni Saf.

600   **Figure 8**: Tsunami simulations for the CFS considering 1.38 m of slip (M_w 7.1 earthquake).

601   The colour scale shows the maximum wave; white contour lines (10 minutes intervals)

602   represent the estimated tsunami travel times. The location of the rupture area is marked in

603   orange on the inset. **a)** Maximum wave amplitudes along the South Spanish and North African

604   coasts, extracted at the 10 m isobath. Selected locations are displayed for reference (Fig. 1).

605   Tsunami simulations considering rake = 0º **(b),** rake = 10º **(c)** and rake = 350º **(d)**. The numbers

606   show the location of the coastal cities taken as reference: 1: Cartagena, 2: Almería, 3:

607   Calahonda, 4: Málaga, 5: Fuengirola, 6: Marbella, 7: La Línea de la Concepción, 8: Ceuta, 9:

608   Alhucemas, 10: Melilla, 11: Beni Saf.

609   **Figure 9:** Tsunami simulations for the YFS considering 1.64 m of slip (M_w 7.3 earthquake).

610   The colour scale shows the maximum wave amplitudes; white contour lines (10 minutes

611   intervals) represent the estimated tsunami travel times. The location of the rupture area is

612   marked in orange on the inset. **a)** Maximum wave amplitudes along the South Spanish and

613   North African coasts, extracted at the 10 m isobath. Selected locations are displayed for

614   reference (Fig. 1). Tsunami simulations considering rake = 0º **(b)**, rake = 190º **(c)** and rake =

615   170º **(d).** The numbers show the location of the coastal cities taken as reference: 1: Cartagena,

616   2: Almería, 3: Calahonda, 4: Málaga, 5: Fuengirola, 6: Marbella, 7: La Línea de la Concepción,

617   8: Ceuta, 9: Alhucemas, 10: Melilla, 11: Beni Saf.

618   **Figure 10:** Tsunami simulations for the AIFS considering 1.13 m of slip (M_w 7 earthquake).

619   The colour scale shows the maximum wave amplitudes; white contour lines (10 minutes

620   intervals) represent the estimated tsunami travel times. **a)** Maximum wave amplitudes along

621   the South Spanish and North African coasts, extracted at the 10 m isobath. Selected locations

622   are displayed for reference (Fig. 1). **b)** Tsunami simulation considering a rectangular

623   approximation of the fault plane. The location of the rupture area is marked in orange on the

624   inset. The numbers show the location of the coastal cities taken as reference: 1: Cartagena, 2:

625   Almería, 3: Calahonda, 4: Málaga, 5: Fuengirola, 6: Marbella, 7: La Línea de la Concepción,

626   8: Ceuta, 9: Alhucemas, 10: Melilla, 11: Beni Saf.

627   **Table 1: (Top)** Instrumental and **(Middle)** historical seismicity nucleated at the Alboran Basin

628   with $M_w > 6$; **(Bottom)** historical tsunamis documented on the Alboran Basin coastal areas

629   associated with a tectonic source in the Alboran Basin.

630   **Table 2:** Acquisition parameters of the Multichannel Seismic (MCS) surveys used to interpret

631   the tectonic structure of the Alboran Basin (Fig. 1): TOPOMED (2011), EVENT-DEEP (2010),

632   EVENT-SHELF (2008), IMPULS (2006), CAB (2000-2001), ESCI (1992), CONRAD (1988).

633   Ch.: channel; CMP: Common Mid-Point.

634   **Table 3:** Fault and rupture parameters and estimated seismogenic potential. Strike, dip and

635   rake variability across the ARFS are shown in Figure 5.

636

637   **References**

638   Álvarez-Gómez, J.A., Aniel-Quiroga, I., González, M., Olabarrieta, M., Carreño, E., 2011a.

639   Scenarios for earthquake-generated tsunamis on a complex tectonic area of diffuse

640   deformation and low velocity: The Alboran Sea, Western Mediterranean. Mar. Geol. 284,

641   55–73. https://doi.org/10.1016/j.margeo.2011.03.008

642   Álvarez-Gómez, J.A., Aniel-Quiroga, I., González, M., Otero, L., 2011b. Tsunami hazard at

643   the Western Mediterranean Spanish coast from seismic sources. Nat. Hazards Earth Syst.

644   Sci. 11, 227–240. https://doi.org/10.5194/nhess-11-227-2011

645   Ballesteros, M., Rivera, J., Muñoz, A., Muñoz-Martín, A., Acosta, J., Carbó, A., Uchupi, E.,

646   2008. Alboran Basin, southern Spain — Part II: Neogene tectonic implications for the

647   orogenic float model. Mar. Pet. Geol. 25, 75–101.

648   Basili, R., Brizuela, B., Herrero, A., Iqbal, S., Lorito, S., Maesano, F.E., Murphy, S., Perfetti,

649   P., Romano, F., Scala, A., Selva, J., Taroni, M., Tiberti, M.M., Thio, H.K., Tonini, R.,

650   Volpe, M., Glimsdal, S., Harbitz, C.B., Løvholt, F., Baptista, M.A., Carrilho, F., Matias,

651   L.M., Omira, R., Babeyko, A., Hoechner, A., Gürbüz, M., Pekcan, O., Yalçıner, A.,

652   Canals, M., Lastras, G., Agalos, A., Papadopoulos, G., Triantafyllou, I., Benchekroun, S.,

653   Agrebi Jaouadi, H., Ben Abdallah, S., Bouallegue, A., Hamdi, H., Oueslati, F., Amato,

654   A., Armigliato, A., Behrens, J., Davies, G., Di Bucci, D., Dolce, M., Geist, E., Gonzalez

655   Vida, J.M., González, M., Macías Sánchez, J., Meletti, C., Ozer Sozdinler, C., Pagani, M.,

656   Parsons, T., Polet, J., Power, W., Sørensen, M., Zaytsev, A., 2021. The Making of the

657   NEAM Tsunami Hazard Model 2018 (NEAMTHM18). Front. Earth Sci. 8.

658   https://doi.org/10.3389/feart.2020.616594

659   Booth-Rea, G., R. Ranero, C., Grevemeyer, I., 2018. The Alboran volcanic-arc modulated the

660   Messinian faunal exchange and salinity crisis. Sci. Rep. 8, 1–14.

661   https://doi.org/10.1038/s41598-018-31307-7

662   Booth-Rea, G., Ranero, C.R., Martínez-Martínez, J.M., Grevemeyer, I., 2007. Crustal types

663   and Tertiary tectonic evolution of the Alborán sea, western Mediterranean. Geochemistry,

664   Geophys. Geosystems 8. https://doi.org/10.1029/2007GC001639

665   Buforn, E., Bezzeghoud, M., Udías, A., Pro, C., 2004. Seismic Sources on the Iberia-African

666   Plate Boundary and their Tectonic Implications. Pure Appl. Geophys. 161, 623–646.

667   https://doi.org/10.1007/s00024-003-2466-1

668   Chen, K., Avouac, J.P., Aati, S., Milliner, C., Zheng, F., Shi, C., 2020. Cascading and pulse-

669   like ruptures during the 2019 Ridgecrest earthquakes in the Eastern California Shear Zone.

670   Nat. Commun. 11, 3–10. https://doi.org/10.1038/s41467-019-13750-w

671   Chertova, M. V., Spakman, W., Geenen, T., van den Berg, A.P., van Hinsbergen, D.J.J., 2014.

672   Underpinning tectonic reconstruction of the western Mediterranean region with dynamic

673   slab evolution from 3-D numerical modeling. J. Geophys. Res. 119, 1–26.

674   https://doi.org/10.1002/2013JB010500.Received

675   d'Acremont, E., Lafosse, M., Rabaute, A., Teurquety, G., Do Couto, D., Ercilla, G., Juan, C.,

676   Mercier de Lépinay, B., Lafuerza, S., Galindo-Zaldívar, J., Estrada, F., Vazquez, J.T.,

677   Leroy, S., Poort, J., Ammar, A., Gorini, C., 2020. Polyphase Tectonic Evolution of Fore

678   - Arc Basin Related to STEP Fault as Revealed by Seismic Reflection Data From the

679   Alboran Sea (W - Mediterranean). Tectonics 39, 1–25.

680   https://doi.org/10.1029/2019TC005885

681   de la Asunción, M., Castro, M.J., Fernández-Nieto, E.D., Mantas, J.M., Acosta, S.O.,

682   González-Vida, J.M., 2013. Efficient GPU implementation of a two waves TVD-WAF

683   method for the two-dimensional one layer shallow water system on structured meshes.

684   Comput. Fluids 80, 441–452. https://doi.org/10.1016/j.compfluid.2012.01.012

685   De Larouzière, F.D., Bolze, J., Bordet, P., Hernandez, J., Montenat, C., Ott d'Estevou, P., 1988.

686   The Betic segment of the lithospheric Trans-Alboran shear zone during the Late Miocene.

687   Tectonophysics 152, 41–52. https://doi.org/10.1016/0040-1951(88)90028-5

688   Duggen, S., Hoernle, K., van den Bogaard, P., Garbe-Schönberg, D., 2005. Post-collisional

689   transition from subduction-to intraplate-type magmatism in the westernmost

690   Mediterranean: Evidence for continental-edge delamination of subcontinental lithosphere.

691   J. Petrol. 46, 1155–1201. https://doi.org/10.1093/petrology/egi013

692   Echeverria, A., Khazaradze, G., Asensio, E., Gárate, J., Dávila, J.M., Suriñach, E., 2013.

693   Crustal deformation in eastern Betics from CuaTeNeo GPS network. Tectonophysics.

694   https://doi.org/10.1016/j.tecto.2013.08.020

695 Elbanna, A., Abdelmeguid, M., Ma, X., Amlani, F., Bhat, H.S., Synolakis, C., Rosakis, A.J.,

696   2021. Anatomy of strike-slip fault tsunami genesis. Proc. Natl. Acad. Sci. 118.

697   https://doi.org/10.1073/PNAS.2025632118

698 Geist, E.L., 2002. Complex earthquake rupture and local tsunamis, JGR, VOL. 107, NO. B5,

699   2086, 10.1029/2000JB000139

700 Gerstenberger, M.C., Marzocchi, W., Allen, T., Pagani, M., Adams, J., Danciu, L., Field, E.H.,

701   Fujiwara, H., Luco, N., Ma, K.F., Meletti, C., Petersen, M.D., 2020. Probabilistic Seismic

702   Hazard Analysis at Regional and National Scales: State of the Art and Future Challenges.

703   Rev. Geophys. 58, 1–49. https://doi.org/10.1029/2019RG000653

704 Giardini, D., Wössner, J., Danciu, L., 2014. Mapping Europe' s Seismic Hazard. Eos, Trans.

705   Am. Geophys. Union 95, 261–268.

706 Goda, K., Mai, P.M., Yasuda, T., Mori, N., 2014. Sensitivity of tsunami wave profiles and

707   inundation simulations to earthquake slip and fault geometry for the 2011 Tohoku

708   earthquake. Earth, Planets Sp. 66, 1–20. https://doi.org/10.1186/1880-5981-66-105

709 Gómez de la Peña, L., 2017. The origin and tectono-sedimentary structure of the Alboran

710   Basin. PhD Thesis, 300 pp. Universitat de Barcelona.

711 Gómez de la Peña, L., Gràcia, E., Muñoz, A., Acosta, J., Gómez-Ballesteros, M., Ranero, C.,

712   Uchupi, E., R. Ranero, C., Uchupi, E., 2016. Geomorphology and Neogene tectonic

713   evolution of the Palomares continental margin (Western Mediterranean). Tectonophysics

714   689, 25–39. https://doi.org/10.1016/j.tecto.2016.03.009

715 Gómez de la Peña, L.G., Ranero, C.R., Gràcia, E., 2018. The Crustal Domains of the Alboran

716   Basin (Western Mediterranean). Tectonics 37, 3352–3377.

717   https://doi.org/10.1029/2017tc004946

718   Gómez de la Peña, L., Grevemeyer, I., Kopp, H., Díaz, J., Gallart, J., Booth- Rea, G., Gràcia,

719   E., R. Ranero, C., 2020. The Lithospheric Structure of the Gibraltar Arc System From

720   Wide- Angle Seismic Data. J. Geophys. Res. Solid Earth 125.

721   https://doi.org/10.1029/2020jb019854

722   Gómez de la Peña, L., R. Ranero, C., Gràcia, E., Booth-Rea, G., 2021. The evolution of the

723   westernmost Mediterranean basins. Earth-Science Rev. 214.

724   https://doi.org/10.1016/j.earscirev.2020.103445

725   González, M., Medina, R., Olabarrieta, M., Otero, L., 2010. Tsunami Hazard Assessment on

726   the Southern Coast of Spain. Turkish J. Earth Sci. 19, 351–366.

727   https://doi.org/10.3906/yer-0812-8

728   Gràcia, E., Bartolome, R., Lo Iacono, C., Moreno, X., Stich, D., Martínez-Diaz, J.J., Bozzano,

729   G., Martínez-Loriente, S., Perea, H., Diez, S., Masana, E., Dañobeitia, J.J., Tello, O., Sanz,

730   J.L., Carreño, E., 2012. Acoustic and seismic imaging of the Adra Fault (NE Alboran

731   Sea): in search of the source of the 1910 Adra earthquake. Nat. Hazards Earth Syst. Sci.

732   12, 3255–3267. https://doi.org/10.5194/nhess-12-3255-2012

733   Gràcia, E., Grevemeyer, I., Bartolomé, R., Perea, H., Martínez-Loriente, S., Gómez de la Peña,

734   L., Villaseñor, A., Klinger, Y., Lo Iacono, C., Diez, S., Calahorrano, A., Camafort, M.,

735   Costa, S., d'Acremont, E., Rabaute, A., Ranero, C.R., 2019. Earthquake crisis unveils the

736   growth of an incipient continental fault system. Nat. Commun. 10, 1–12.

737   https://doi.org/10.1038/s41467-019-11064-5

738   Gràcia, E., Pallàs, R., Soto, J.I., Comas, M., Moreno, X., Masana, E., Santanach, P., Diez, S.,

739   García, M., Dañobeitia, J., 2006. Active faulting offshore SE Spain (Alboran Sea):

740   Implications for earthquake hazard assessment in the Southern Iberian Margin. Earth

741   Planet. Sci. Lett. 241, 734–749. https://doi.org/10.1016/j.epsl.2005.11.009

742   Grevemeyer, I., Gràcia, E., Villaseñor, A., Leuchters, W., Watts, A.B., 2015. Seismicity and

743   active tectonics in the Alboran Sea, Western Mediterranean: Constraints from an offshore-

744   onshore seismological network and swath bathymetry data. J. Geophys. Res. Solid Earth

745   120, 767–787. https://doi.org/10.1002/2015JB012352.

746   Herrero, A., Murphy, S., 2018. Self-similar slip distributions on irregular shaped faults.

747   Geophys. J. Int. 213, 2060–2070. https://doi.org/10.1093/gji/ggy104

748   IGN, 2013. Catálogo de tsunamis de las costas españolas.

749   https://www.ign.es/web/resources/docs/IGNCnig/SIS-Catalogo-Tsunamis-Costas-

750   Espanolas.pdf

751   IGN seismic catalogue: http://www.ign.es/ (last access on May 2021).

752   Kaabouben, F., Baptista, M.A., Iben Brahim, A., El Mouraouah, A., Toto, A., 2009. On the

753   moroccan tsunami catalogue. Nat. Hazards Earth Syst. Sci. 9, 1227–1236.

754   https://doi.org/10.5194/nhess-9-1227-2009

755   Leonard, M., 2014. Self-consistent earthquake fault-scaling relations: Update and extension to

756   stable continental strike-slip faults. Bull. Seismol. Soc. Am. 104, 2953–2965.

757   https://doi.org/10.1785/0120140087

758   Maesano, F. E., and D'Ambrogi, C., 2017. Vel-IO 3D: a tool for 3D velocity model

759   construction, optimization and time-depth conversion in 3D geological modeling

760   workflow. Comput. Geosci. 99, 171–182. doi: 10.1016/j.cageo.2016.11.013

761   Mancilla, F. de L., Booth-Rea, G., Stich, D., Pérez-Peña, J.V., Morales, J., Azañón, J.M.,

762   Martin, R., Giaconia, F., 2015. Slab rupture and delamination under the Betics and Rif

763   constrained from receiver functions. Tectonophysics 663, 225–237.

764   https://doi.org/10.1016/j.tecto.2015.06.028

765   Maramai, A., Brizuela, B., Graziani, L., 2014. The Euro-Mediterranean Tsunami Catalogue.

766   Ann. Geophys. 57, S0435. https://doi.org/10.4401/ag-6437

767   Martín, R., Stich, D., Morales, J., Mancilla, F., 2015. Moment tensor solutions for the Iberian-

768   Maghreb region during the IberArray deployment (2009-2013). Tectonophysics 663,

769   261–274. https://doi.org/10.1016/j.tecto.2015.08.012

770   Martínez-García, P., Comas, M., Soto, J.I., Lonergan, L., Watts, A. B., 2013. Strike-slip

771   tectonics and basin inversion in the Western Mediterranean: the Post-Messinian evolution

772   of the Alboran Sea. Basin Res. 25, 361–387. https://doi.org/10.1111/bre.12005

773   Mezcua, J., Rueda, J., Blanco, R.M.G., 2004. Reevaluation of historic Earthquakes in Spain.

774   Seismol. Res. Lett. 75, 75–81. https://doi.org/10.1785/gssrl.75.1.75

775   Moreno, X., Gràcia, E., Bartolomé, R., Martínez-Loriente, S., Perea, H., Gómez de la Peña, L.,

776   Iacono, C. Lo, Piñero, E., Pallàs, R., Masana, E., Dañobeitia, J.J., 2016.

777   Seismostratigraphy and tectonic architecture of the Carboneras Fault offshore based on

778   multiscale seismic imaging: Implications for the Neogene evolution of the NE Alboran

779   Sea. Tectonophysics 689, 115–132. https://doi.org/10.1016/j.tecto.2016.02.018

780   Murphy, S., Scala, A., Herrero, A., Lorito, S., Festa, G., Trasatti, E., Tonini, R., Romano, F.,

781   Molinari, I., Nielsen, S., 2016. Shallow slip amplification and enhanced tsunami hazard

782   unravelled by dynamic simulations of mega-thrust earthquakes. Sci. Rep. 6, 1–12.

783   https://doi.org/10.1038/srep35007

784   Nocquet, J.-M., 2012. Present-day kinematics of the Mediterranean: A comprehensive

785   overview of GPS results. Tectonophysics 579, 220–242.

786   https://doi.org/10.1016/j.tecto.2012.03.037

787   Palano, M., González, P.J., Fernández, J., 2013. Strain and stress fields along the Gibraltar

788   Orogenic Arc: Constraints on active geodynamics. Gondwana Res. 23, 1071–1088.

789   https://doi.org/10.1016/j.gr.2012.05.021

790   Palano, M., González, P.J., Fernández, J., 2015. The Diffuse Plate boundary of Nubia and

791   Iberia in the Western Mediterranean: Crustal deformation evidence for viscous coupling

792   and   fragmented   lithosphere.   Earth   Planet.   Sci.   Lett.   430,   439–447.

793   https://doi.org/10.1016/j.epsl.2015.08.040

794   Passone, L., Mai, P. M., 2017. Kinematic earthquake Ground-Motion simulations on listric

795   normal   faults.   Bull.   Seismol.   Soc.   Am.   107,   2980–2993.

796   https://doi.org/10.1785/0120170111

797   Perea, H., Gràcia, E., Almeida, S., Gómez de la Peña, L., Martínez-Loriente, S., Bartolomé, R.,

798   2020. Revealing the earthquake history during the last 200 ka on a large submarine strike-

799   slip fault: The Yusuf Fault System (Alboran Sea). EGU General Assembly.

800   https://doi.org/10.5194/egusphere-egu2020-13362

801   Ruiz, J.A., Baumont, D., Bernard, P., Berge-Thierry, C., 2011. Modelling directivity of strong

802   ground motion with a fractal, k-2, kinematic source model. Geophys. J. Int. 186, 226–244.

803   https://doi.org/10.1111/j.1365-246X.2011.05000.x

804   Scala, A., Lorito, S., Romano, F., Murphy, S., Selva, J., Basili, R., Babeyko, A., Herrero, A.,

805   Hoechner, A., Løvholt, F., Maesano, F.E., Perfetti, P., Tiberti, M.M., Tonini, R., Volpe,

806   M., Davies, G., Festa, G., Power, W., Piatanesi, A., Cirella, A., 2020. Effect of Shallow

807   Slip Amplification Uncertainty on Probabilistic Tsunami Hazard Analysis in Subduction

808   Zones: Use of Long-Term Balanced Stochastic Slip Models. Pure Appl. Geophys. 177,

809   1497–1520. https://doi.org/10.1007/s00024-019-02260-x

810   Sahal, A., Roger, J., Allgeyer, S., Lemaire, B., Hébert, H., Schindelé, F., Lavigne, F., 2009.

811   The tsunami triggered by the 21 May 2003 Boumerdès-Zemmouri (Algeria) earthquake:

812   Field investigations on the French mediterranean coast and tsunami modelling. Nat.

813   Hazards Earth Syst. Sci. 9, 1823–1834. https://doi.org/10.5194/nhess-9-1823-2009

814   Selva, J., Lorito, S., Volpe, M., Romano, F., Tonini, R., Perfetti, P., Bernardi, F., Taroni, M.,

815   Scala, A., Babeyko, A., Løvholt, F., Gibbons, S.J., Macías, J., Castro, M.J., González-

816   Vida, J.M., Sánchez-Linares, C., Bayraktar, H.B., Basili, R., Maesano, F.E., Tiberti,

817   M.M., Mele, F., Piatanesi, A., Amato, A., 2021. Probabilistic tsunami forecasting for early

818   warning. Nat. Commun. 12. https://doi.org/10.1038/s41467-021-25815-w

819   Serra, C. S., Martínez-Loriente, S., Gràcia, E., Urgeles, R., Gómez de la Peña, L., Maesano, F.

820   E., Basili, R., Volpe, M., Romano, F., Scala, A., Piatanesi, A., Lorito, S. 2021. Sensitivity

821   of tsunami scenarios to complex fault geometry and heterogeneous slip distribution: Case

822   studies for SW Iberia and NW Morocco. Journal of Geophysical Research: Solid Earth,

823   126, e2021JB022127. https://doi.org/10.1029/2021JB022127.

824   Serpelloni, E., Vannucci, G., Pondrelli, S., Argnani, A., Casula, G., Anzidei, M., Baldi, P.,

825   Gasperini, P., 2007. Kinematics of the Western Africa-Eurasia plate boundary from focal

826   mechanisms   and   GPS   data.   Geophys.   J.   Int.   169,   1180–1200.

827   https://doi.org/10.1111/j.1365-246X.2007.03367.x

828   Stich, D., Ammon, C.J., Morales, J., 2003. Moment tensor solutions for small and moderate

829   earthquakes   in   the   Ibero-Maghreb   region.   J.   Geophys.   Res.   108,   2148.

830   https://doi.org/10.1029/2002JB002057

831   Stucchi et al., 2013. The SHARE European Earthquake Catalogue (SHEEC) 1000–1899.

832   Journal of Seismology, doi: 10.1007/s10950-012-9335-2.

833   Tanioka, Y., Satake, K., 1996. Tsunami generation by horizontal displacement of ocean

834   bottom. Geophys. Res. Lett. 23, 861–864. https://doi.org/10.1029/96GL00736

835   Tonini, R., Basili, R., Maesano, F.E., Tiberti, M.M., Lorito, S., Romano, F., Scala, A., Volpe,

836   M., 2020. Importance of earthquake rupture geometry on tsunami modelling: The

837   Calabrian Arc subduction interface (Italy) case study. Geophys. J. Int. 223, 1805–1819.

838   https://doi.org/10.1093/gji/ggaa409

839   Ulrich, T., Gabriel, A.A., Ampuero, J.P., Xu, W., 2019. Dynamic viability of the 2016 Mw 7.8

840   Kaikōura earthquake cascade on weak crustal faults. Nat. Commun. 10.

841   https://doi.org/10.1038/s41467-019-09125-w

842   Wortel, M.J., Spakman, W., 2000. Subduction and slab detachment in the Mediterranean-

843   Carpathian region. Science 290, 1910–1917.

844   https://doi.org/10.1126/science.290.5498.1910

845   Zeng, Y., Anderson, J.G., Yu, G., 1994. A composite source model for computing realistic

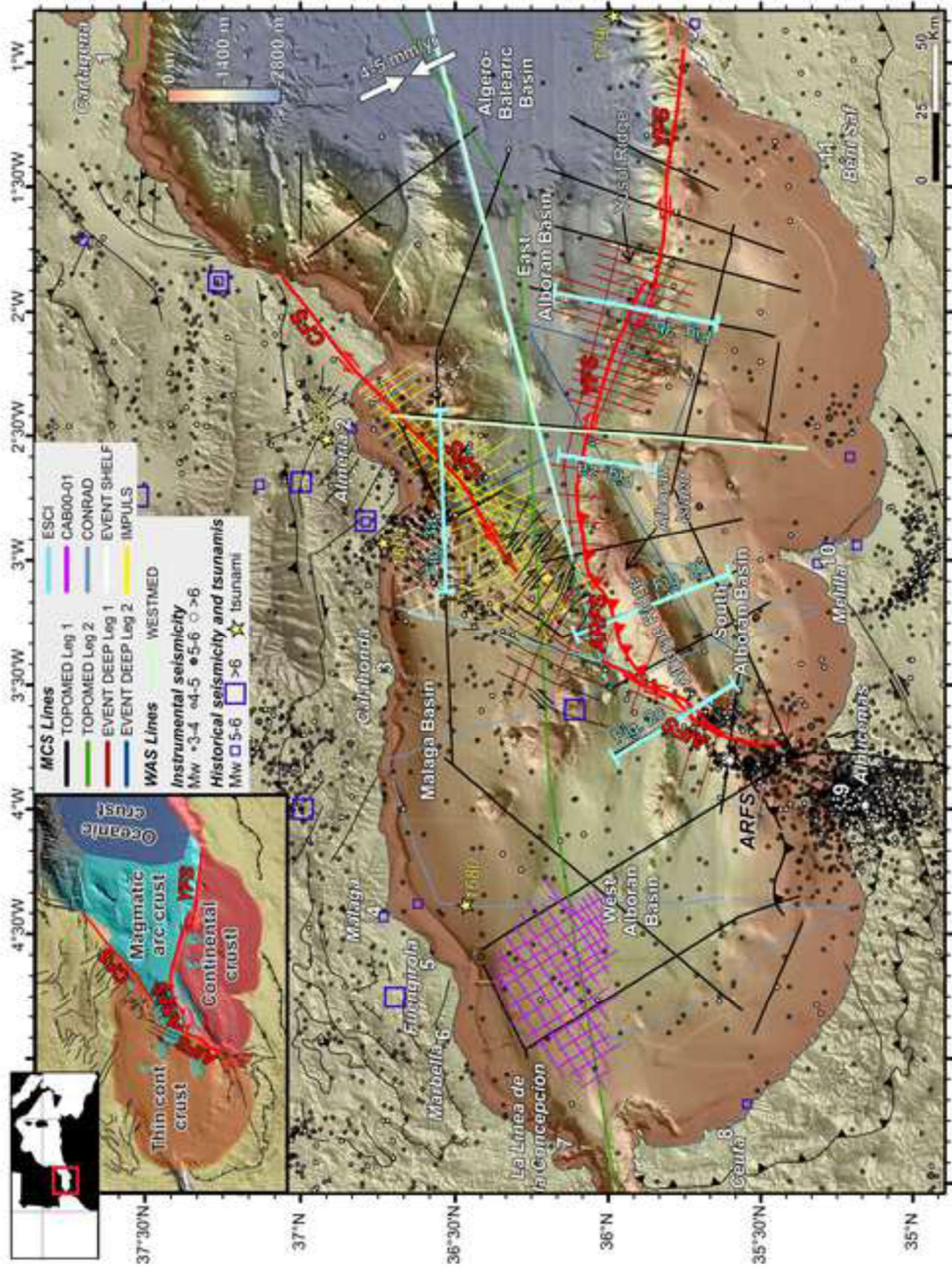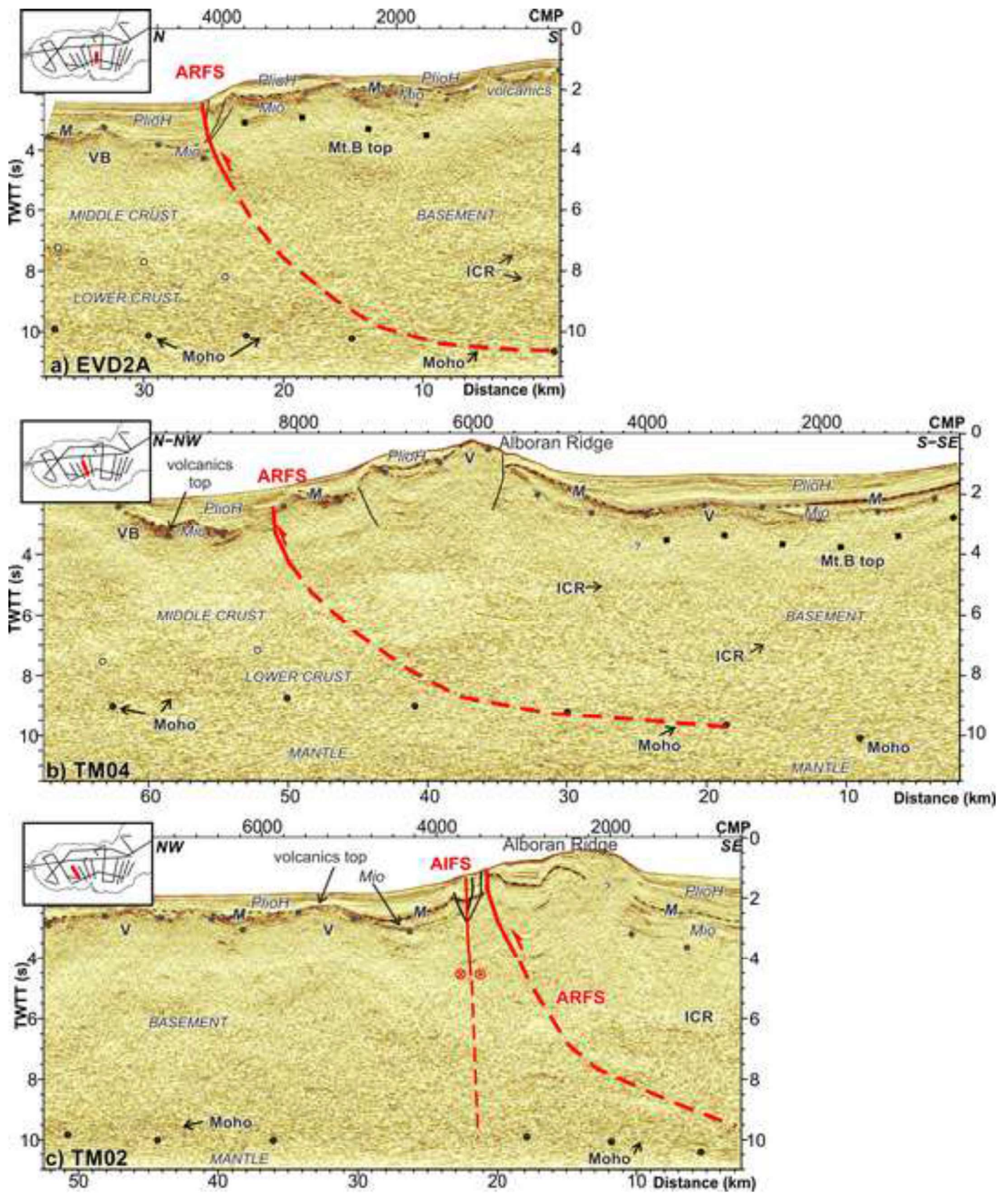846   synthetic strong ground motions. Geophys. Res. Lett. 21, 725–728.

Figure 1

Figure 2

Figure 3

Figure 4

Figure 5

a) Strike

b) Dip

c) Rake

Figure 6

a)

c) Realistic geometry - constant rake
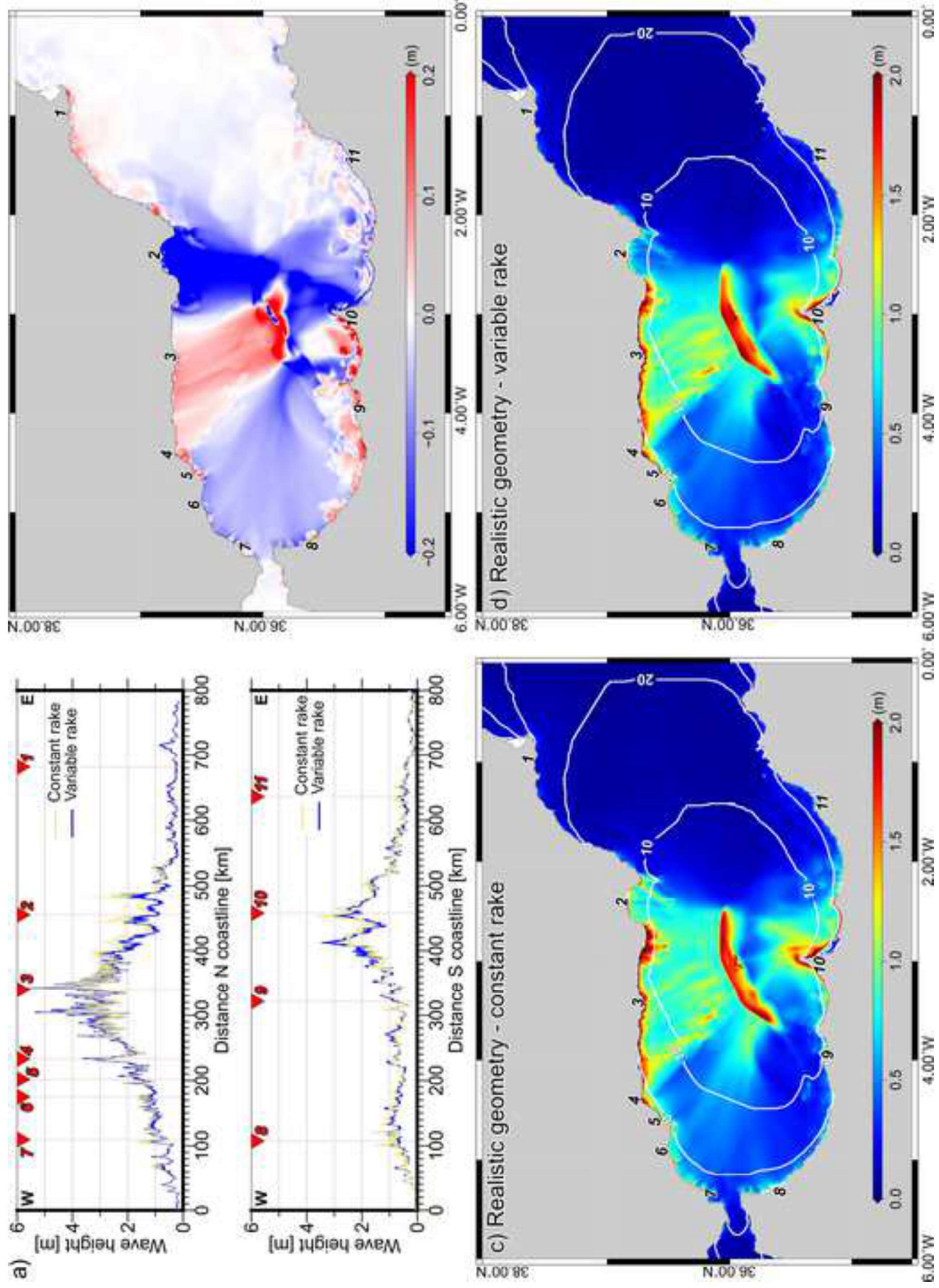
d) Realistic geometry - variable rake

Figure 7

Figure 8

Figure 9

a) Wave height [m] vs Distance N coastline [km] and Distance S coastline [km], with Rake 190°, Rake 180°, Rake 170°

b) Rectangular approximation Rake = 180°

c) Rectangular approximation Rake = 190°

d) Rectangular approximation Rake = 170°
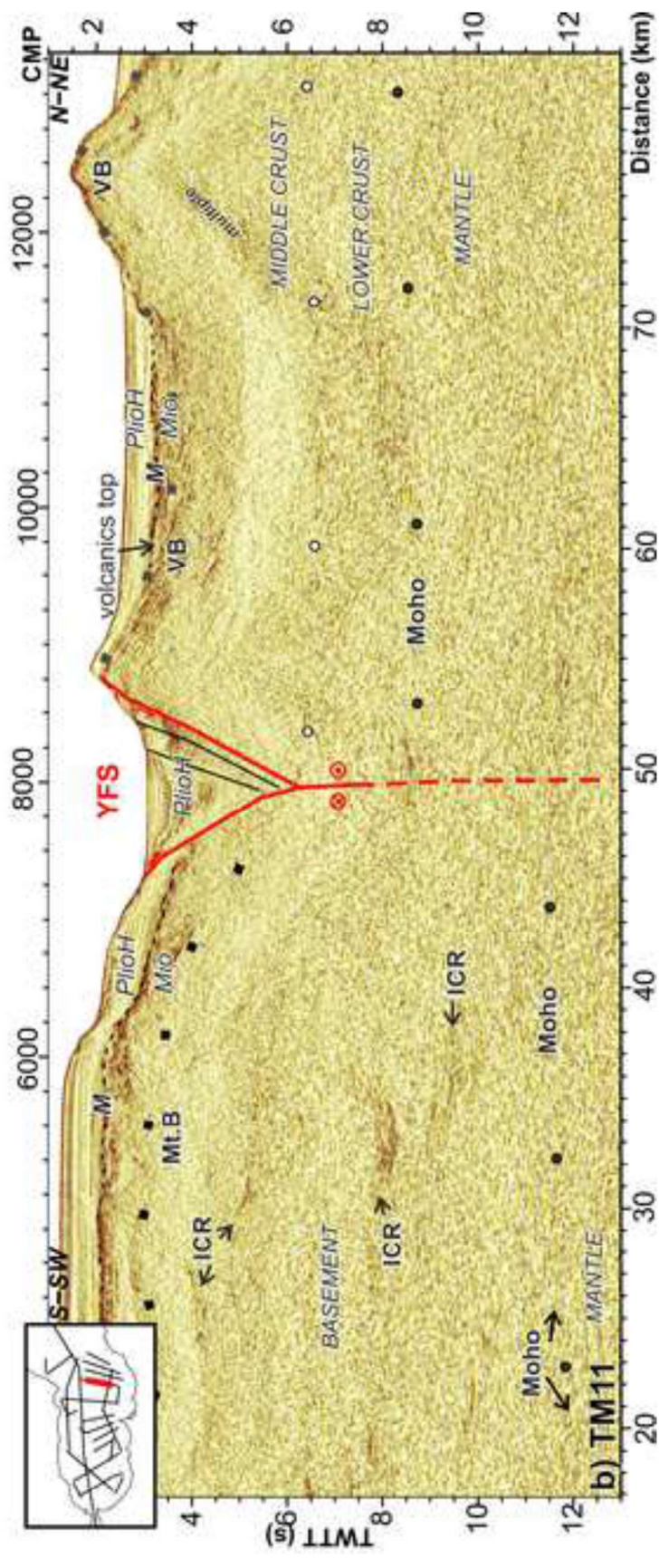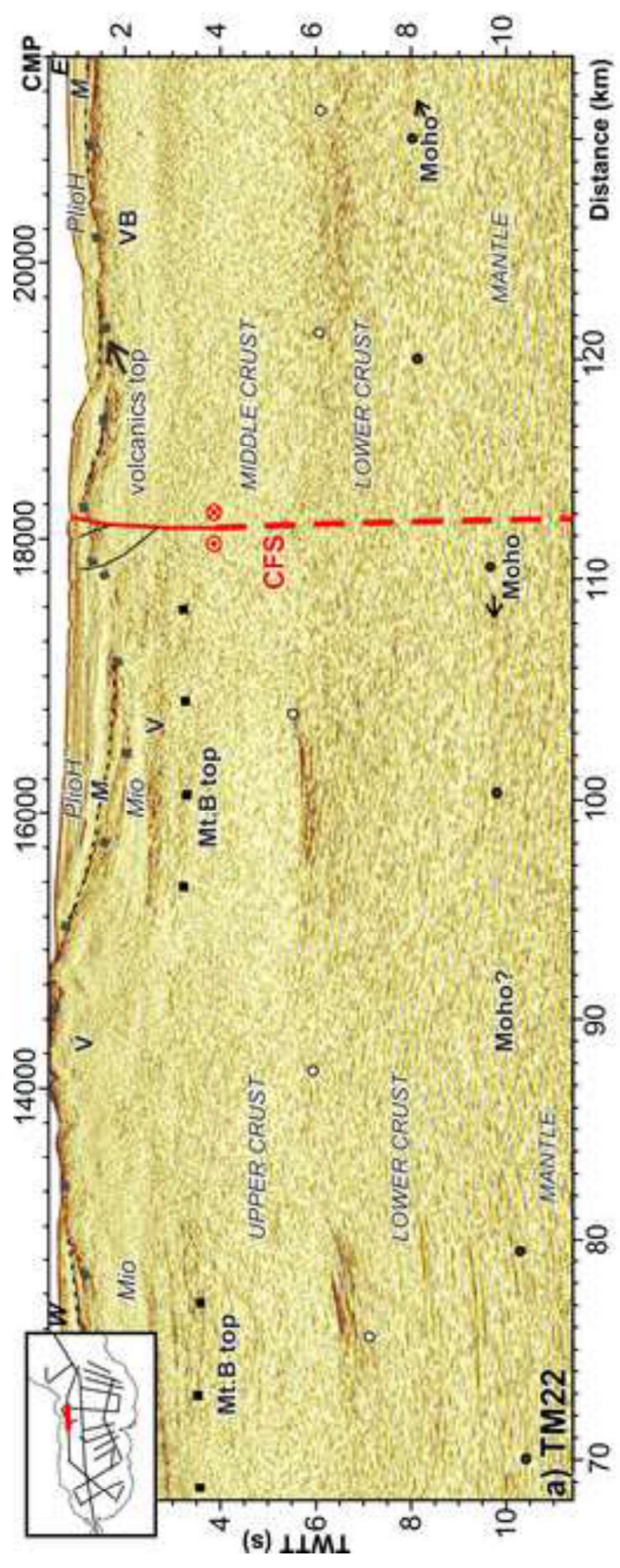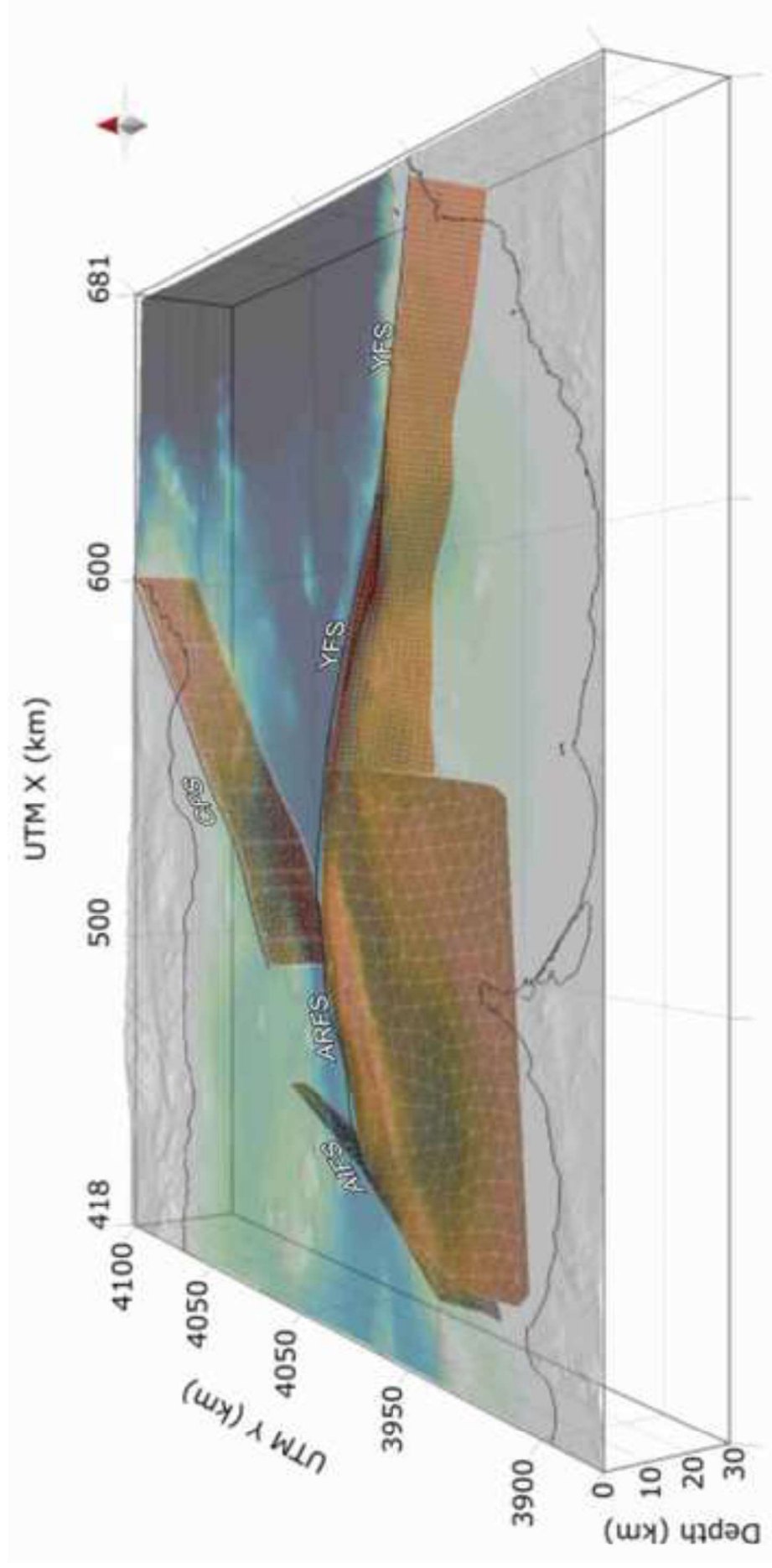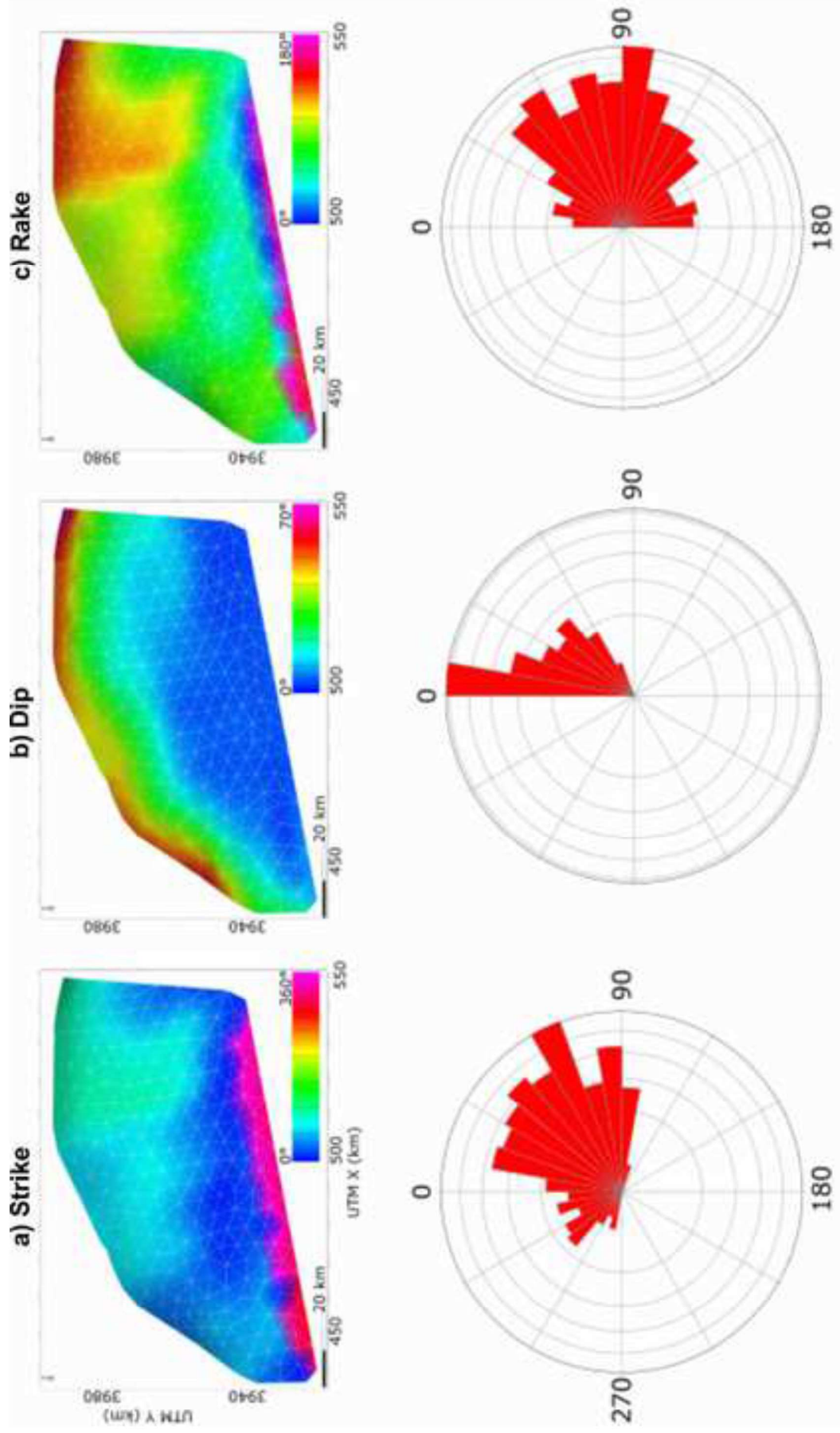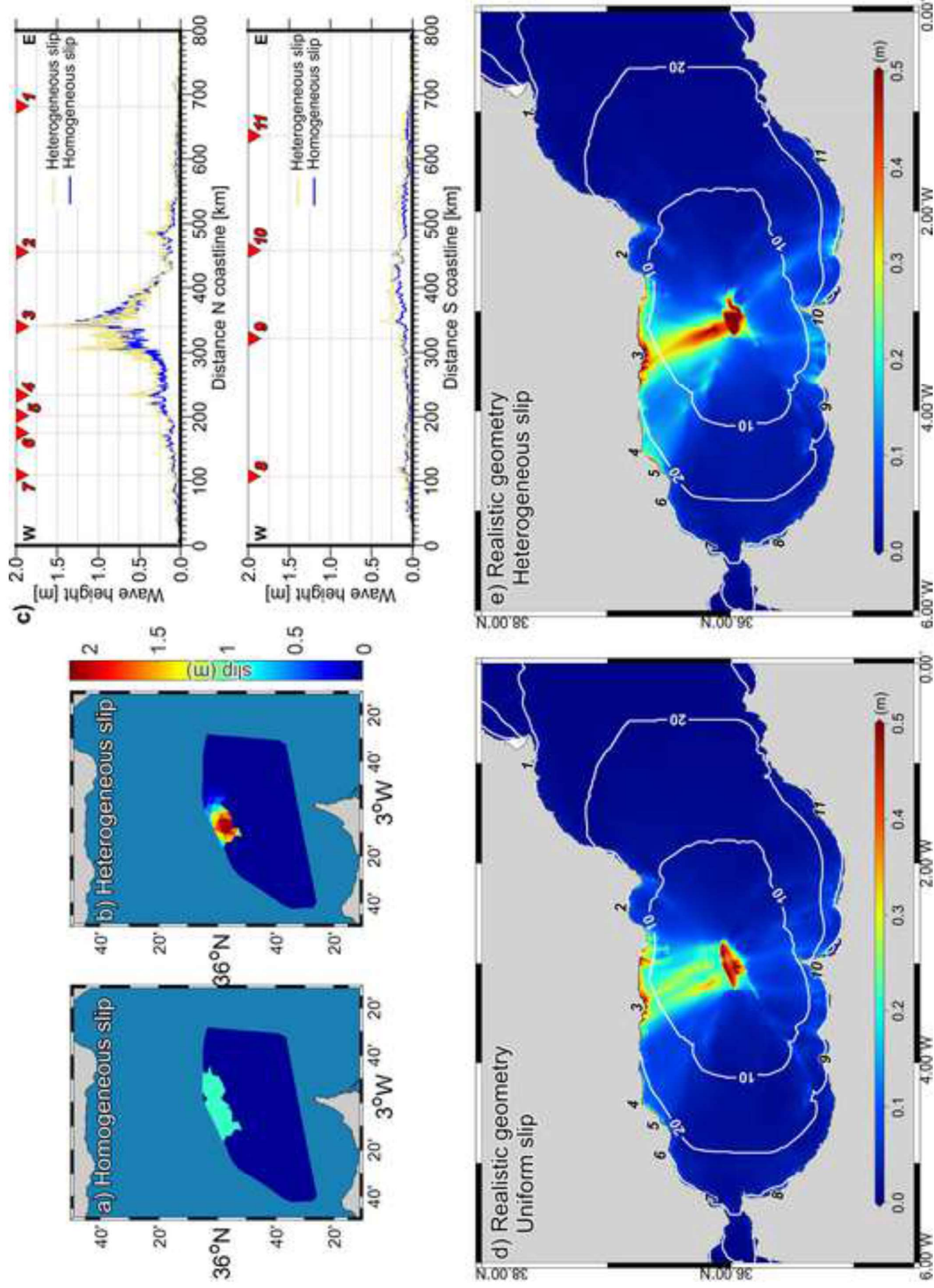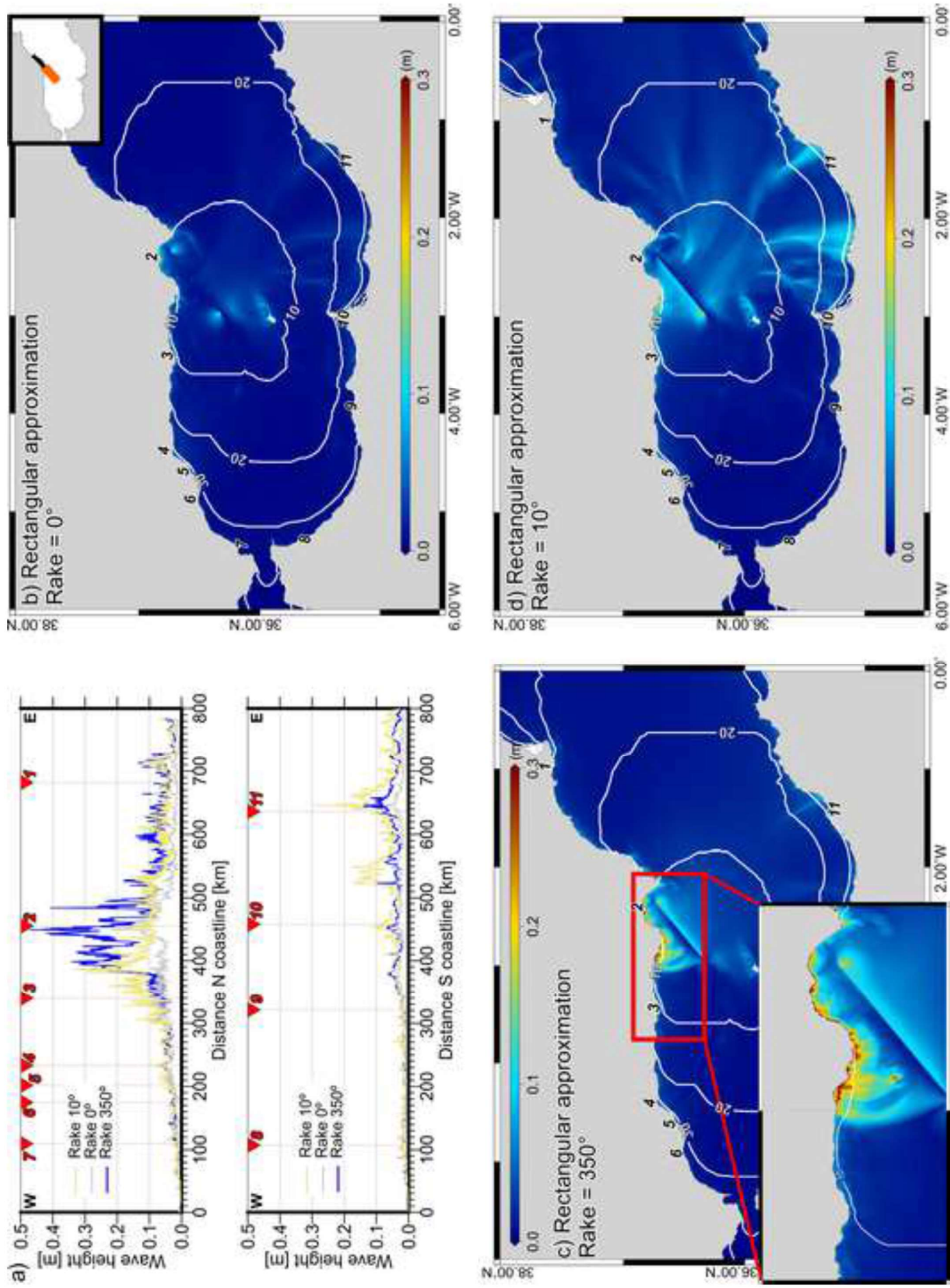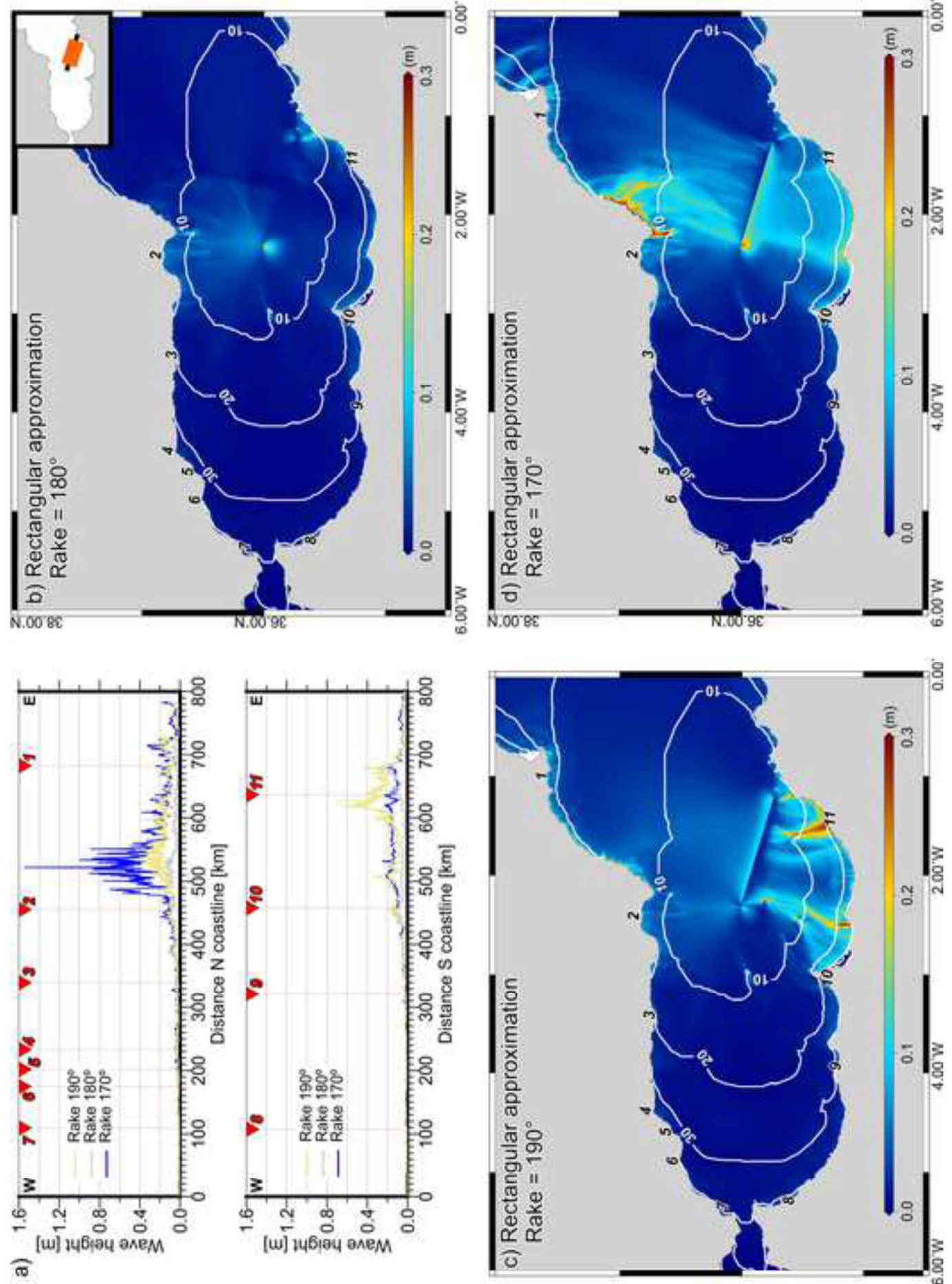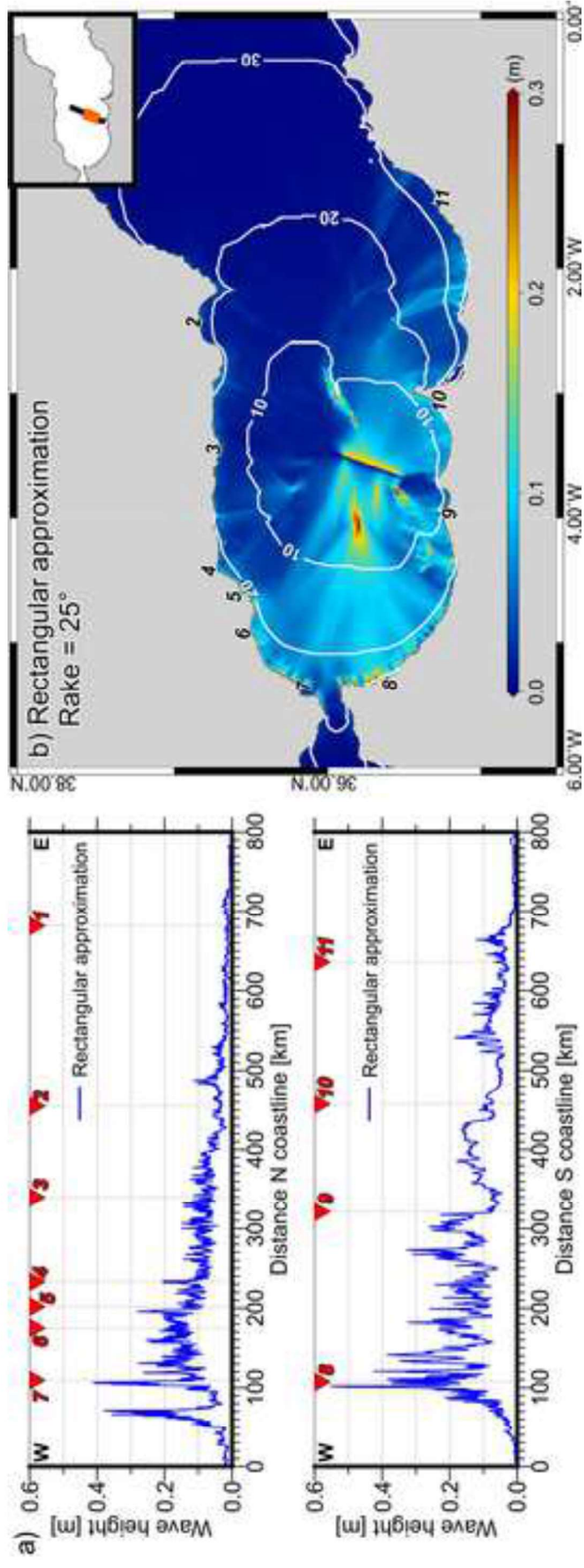
Figure 10

Instrumental seismicity $M_w > 6$							
Year	M_w	Lat.	Long.	Prof. (km)	Max. Intensity	Effects	References
2016	6.4	35.59	-3.72	10	VI	1 casualty, 30 injured, material damages in S. Spain and N. Morocco coastal cities.	*Gràcia et al., 2019*
2004*	6.3	35.15	-3.98	-	VIII	629 casualties, material damage. Most catastrophic earthquake in the region in the last 100 years.	*IGN seismic catalogue*

* The 2004 earthquake occurred onshore and was nucleated on the onshore continuation of the AIFS.

Historical seismicity $M_w > 6$					
Year	Estimated M_w	Lat.	Long.	Max. Intensity	References
1804	6.7	36.02	-3.79	VII-VIII	*Mezcua et al., 2004*
1804*	6.4	36.59	-2.83	VIII-IX	*Mezcua et al., 2004*
1790	6.7	35.70	-0.60	-	*Kaabouben et al., 2009*
1680	7	36.30	-4.24	IX	*Kaabouben et al., 2009*
1522	6.5	36.97	-2.66	-	*Kaabouben et al., 2009*

* The 1804 earthquake occurred onshore and was probably nucleated on the onshore continuation of the CFS. They are interpreted as two different events on the seismic catalogues, being the tsunamigenic one the M_w 6.7 earthquake, nucleated offshore.

Historical tsunamis related to a tectonic source in the Alboran Basin						
Year	Affected area	Documented effects	Possible source			References
			M_w	Int.	Lat.	Long.	
1804	Almeria province	Sea retreat	-	VII	36.50	-2.50	*IGN tsunami catalogue*
1790	Almeria province, Algeria	Noticeable inundation distance in Almeria in the dry land	6.7	-	35.70	-0.6	*Kaabouben et al., 2009*
1680	Malaga, North of Morocco	Sea rise of 5 m	7	IX	36.30	-4.24	*Kaabouben et al., 2009*
1522	Bades Ghomera, Almeria province	-	6.5	-	36.97	-2.66	*Kaabouben et al., 2009*

Table 1

Table 2

Survey	Ch.	Ch. Distance (m)	Streamer length (m)	CMP distance (m)	Sample rate (ms)	Recorded length (s)	Shot distance (m)	Airguns volume
TOPOMED 1	408	12.5	5397	6.25	2	12/14	37.5/50	2000 psi
TOPOMED 2	480	12.5	6332	6.25	2	19	50	2500 psi
EVENT-DEEP 1	96	6.25	600	3.125	2	5.5/8	12.5/18.7	800 c.i.
EVENT-DEEP 2	276	12.5	3450	6.25	2	12	37.5	1880 c.i.
EVENT-SHELF	1	-	9	-	0.1	1.5/2.0	~15	sparker
IMPULS	48	6.25	300	3.125	1	12/6	25/12.5	800 c.i.
CAB	480	12.5	6000	6.25	2	12	37.5	2800 c.i.
ESCI	180	25	4500	12.5	4	18/22	50/75	7118 c.i.
CONRAD	48	50	2400	25	4	20	50	5346 c.i.

Table 2

Table 3

Fault	Fault parameters			Rupture dimensions		Centre of the rupture			Seismogenic potential	
Fault	Strike	Dip	Rake	Length (km)	Width (km)	Lat.	Long.	Depth (km)	Slip (m)	Mw
ARFS (all)	complex	complex	80/ complex	120	42	Determined by the 3D mesh			2.66	7.7
ARFS (ramp)	complex	complex	80	45	22	Determined by the 3D mesh			0.92 Up to 2.13*	6.8
CFS	230	90	0	71	20	-2.66	36.53	11	1.38	7.1
YFS	107	81	180	102	22	-1.78	35.53	11.5	1.64	7.3
AIFS	20	90	25	47.5	17	-3.59	35.70	9	1.13	7.0

* Heterogeneous slip distribution (Fig. 7b).

Table 3